Preprints.org

Article

Not peer-reviewed version

Hydrogeochemical Characteristics of Earthquake-Related varied-temperature Springs along the Eastern Kunlun Fault Zone, China

Chao Lu , Xiaocheng Zhou * , Jiyi Jiang * , Jingchao Li , Jing Li , Jing Wu , Xiaoyi Zhu , Jiang Li , Gaoyuan Xing , Shihan Cui

Posted Date: 19 March 2024

doi: 10.20944/preprints202403.1101.v1

Keywords: varied-temperature water; hydrogeochemistry; isotopes; seismic precursor; Eastern Kunlun Fault

Preprints.org is a free multidiscipline platform providing preprint service that is dedicated to making early versions of research outputs permanently available and citable. Preprints posted at Preprints.org appear in Web of Science, Crossref, Google Scholar, Scilit, Europe PMC.

Copyright: This is an open access article distributed under the Creative Commons Attribution License which permits unrestricted use, distribution, and reproduction in any medium, provided the original work is properly cited.

Preprints.org (www.preprints.org) | NOT PEER-REVIEWED | Posted: 19 March 2024 doi:10.20944/preprints202403.1101.v1

Disclaimer/Publisher's Note: The statements, opinions, and data contained in all publications are solely those of the individual author(s) and contributor(s) and not of MDPI and/or the editor(s). MDPI and/or the editor(s) disclaim responsibility for any injury to people or property resulting from any ideas, methods, instructions, or products referred to in the content.

Article

Hydrogeochemical Characteristics of Earthquake-Related Varied-Temperature Springs Along the Eastern Kunlun Fault Zone, China.

Chao Lu [1], Xiaocheng Zhou [2,3,] *, Jiyi Jiang [1,4,] *, Jingchao Li [2], Jing Li [1], Jing Wu [5], Xiaoyi Zhu [2], Jiang Li [2], Gaoyuan Xing [2] and Shihan Cui [2]

[1] School of Ecological Environment, Institute of Disaster Prevention, Sanhe 065201, China; luchao76b1122@163.com (C.L.); 102lij@163.com (J.L.)
[2] United Laboratory of High-Pressure Physics and Earthquake Science, Institute of Earthquake Forecasting, China Earthquake Administration, Beijing 100036, China; lijc@ief.ac.cn (J.L.); zxy_bj2008@126.com (X.Z.); lijiang@ief.ac.cn (J.L.); xinggy2219@163.com (G.X.); c1416102468@163.com (S.C.)
[3] School of Earth Sciences and Resources, China University of Geosciences, Beijing 100083, China
[4] Hebei Key Laboratory of Earthquake Dynamics, Sanhe 065201, China
[5] Earthquake Administration of Shandong Province, Jinan 250014, China; dzj_huiyang@163.com (J.W.)
* Correspondence: zhouxiaocheng188@163.com (X.Z.); jiangjiyi@cidp.edu.cn (J.J.)

Abstract: The Eastern Kunlun Fault Zone (EKFZ) is located in a seismic blank area. This study investigates the hydrogeochemical characteristics of varied-temperature springs (i.e., springs exhibiting temperatures from cold to hot due to diverse geothermal gradients and groundwater circulation depths) in the EKFZ to understand the relationship between fractures, fluids, and earthquakes. It aids in establishing their induction mechanisms and assists in monitoring the earthquake precursors of the EKFZ. In this study, the main elements, trace elements, hydrogen and oxygen isotopes, and strontium isotopes of 23 varied-temperature springs in the EKFZ were analyzed. The results reveal the source of groundwater recharge, hydrochemical types, mineral saturation, and for a select few springs indicative of geothermal activity, collected geothermal reservoir temperatures. This study also explores the relationship between earthquakes and springs, identifying sensitive chemical indicators. Based on continuous monitoring at Maqu Station, we found that before the occurrence of the Maerkang *M*s 6.0 earthquake, the concentration of Cl^- rose by 2.9 times, and 46 days before the Gande earthquake (*M*s = 4.7), the concentrations of Na^+ and SO_4^{2-} significantly increased. Finally, a conceptual model of the hydrogeochemistry of springs is presented to describe the groundwater circulation in the study area. This research is of great significance for the analysis of fluid geochemistry in this area and for assessing the seismic hazards of the EKFZ.

Keywords: varied-temperature water; hydrogeochemistry; isotopes; seismic precursor; Eastern Kunlun Fault

1. Introduction

Springs are a window to deep crustal changes [1]. A seismically active fault provides upwelling conduits for fluids in active tectonic settings [1–3]. The distribution and connectivity of fault systems control fluid circulation, and fault properties play a significant role in determining circulation depth and fluid geochemical composition [4–6]. Furthermore, stress accumulation, changes in stress state, and variations in thermal dynamic conditions can alter the balance of the water–rock system [7]. In recent years, research has increasingly focused on investigating the connection between hydrogeochemistry and earthquakes [8–11]. For example, before and after the 2019 Benevento earthquake in Italy, anomalies in water chemistry were observed, including increased dissolved CO_2

© 2024 by the author(s). Distributed under a Creative Commons CC BY license.

Preprints.org (www.preprints.org) | NOT PEER-REVIEWED | Posted: 19 March 2024 doi:10.20944/preprints202403.1101.v1

levels, decreased pH, and abnormal concentrations of major ions (Ca^{2+}, Na^{+}, HCO_3^{-}, etc.), which returned to their typical concentrations after the earthquake [12]. Similarly, before the 1995 Galicia earthquake in Spain, the concentration of Cl^{-} in the water doubled [13]. Moreover, some trace elements such as Pb, B, etc., may also show changes prior to earthquakes [14].

The Eastern Kunlun Fault (EKF), situated in the northern part of the Tibetan Plateau, has been highly active in the late Quaternary and has experienced six earthquakes of magnitude 7–8 in its history [14]. Three earthquakes, including the Maerkang M_S 6.0 earthquake, the Gande M_S 4.7 earthquake, and the Maduo M_S 5.0 earthquake, occurred near the EKFZ during continuous monitoring. Notably, the Maqin and Maqu sections within the Eastern Kunlun Fault Zone are considered seismic gap regions with a significant population density, which poses potential threats to the safety of life and property in this area [15–18]. However, previous research on the Eastern Kunlun Fault Zone (EKLF) has predominantly focused on geological and tectonic aspects, rock formation, ore deposit geology, and geochemical characteristics. There has been limited research in the field of hydrogeochemistry, particularly regarding the chemical composition of waters in the eastern part of the EKFZ region and the mechanisms underlying the evolution of water chemistry over an extended period.

Examining the hydrological and geochemical changes during earthquake occurrences can assist in understanding the relationship between earthquakes and fluid geochemistry, identifying earthquake activity, and monitoring water chemistry in highly seismically active areas [19,20]. The objective of this research is to examine the hydrogeochemical properties of varied-temperature springs (i.e., springs exhibiting temperatures from cold to hot due to diverse geothermal gradients and groundwater circulation depths) and identify potential earthquake-prone areas in the east-central section of the EKFZ. This study will create a hydrogeochemical cycle model of springs to understand the interaction between deep and shallow fluids within the fault zone. By investigating the fluid geochemical characteristics of springs and their relationship with earthquakes, this study, combined with the time-dependent variations in the chemical composition of three springs which have been continuously monitored since June 2021, will contribute to predicting possible earthquakes in the EKFZ for future reference.

2. Geological Setting

The EKFZ, stretching approximately 500 km, acts as the boundary between the Bayankhara crustal blocks and Kunlun Qaidam in the northern region of the Tibetan Plateau (see Figure 1). The study area exhibits various structural features, including the Jungong fault, the intersection zone of the Xigongzhou Fault, the uplift of the A'nyêmaqên Mountains, and the Maqu section intersection with the Minjiang Fault. Additionally, the Huya Fault forms a horsetail-shaped contraction structure. Within the research area, geomorphic features like the Xigongzhou and Mohatang basins, Min Mountain uplift, and single-faulted basins (Maqin and Maqu basins) have led to the accumulation of stress in the mid-eastern section of the EKFZ [21]. The fault itself has a dip angle ranging from 60° to 80° and strikes predominantly at 280°–310°, with a southwestward dip. The eastern section of the EKFZ is a large strike-slip fault consisting of three main segments, namely, Maqu, Maqin, and Tuosuohu, from east to west. The Tuosuohu segment is situated to the west of the A'nyêmaqên Mountains and exhibits a sinistral slip rate of 4.0–10.9 mm/a (millimeters per year) [21–23]. Its strike direction is between 280° and 290°. The Maqin segment extends over an approximate distance of 110 km, exhibiting a northwest–southeast orientation. It begins in the Yangkao gully, passes through Dongqinggou, Rirang, Dawutan, Dawumuchang, and ends in eastern Kendingna. Since the late Pleistocene, its slip rate has been estimated at 6.0–12.5 mm/a [21–24]. The Maqu segment extends for 110 km with a dip angle ranging from 60° to 75°, striking at 280°–305°. It originates from Mohatang, traverses through Awancang Fault, Halawen, Tangdi, and Keshengtuoluo, and terminates in the south of Maqu County. Li et al. provided information regarding the long-term horizontal slip rate of the EKFZ since the beginning of the late Quaternary (as shown in Table 1) [15]. The sliding rate of the EKFZ gradually increases from east to west.

Preprints.org (www.preprints.org) | NOT PEER-REVIEWED | Posted: 19 March 2024 doi:10.20944/preprints202403.1101.v1

The mid-eastern part of the EKFZ has experienced several significant earthquakes, according to historical records. Over the past century, the Tuosuohu segment has been struck by three major earthquakes, with the most recent being the Tuosuohu M_S 7.5 earthquake in 1937. The recurrence period for earthquakes in this segment is estimated to be 630 ± 130 years over the last 2000 years [21,25]. In the Maqin sector, there have been seven major earthquakes in the past 10,000 years, with the most recent occurring in 534 BC. The recurrence interval for Maqin earthquakes is approximately 600 ± 100 years in the most recent 2000 years [21,26,27]. Compared to the Maqin and Tuosuohu sections, the seismic activity in the Maqu region is notably diminished, with the most recent earthquake occurring approximately 1055 years ago. The recurrence interval for Maqu earthquakes is estimated to be 1000 years [28]. The temporal and spatial sequence of earthquakes in the three sections (Maqin, Maqu, and Tuosuohu) suggests an interaction between them. Coseismic dislocations in the southeast section generate stress–strain loading on adjacent sections, leading to the triggering or acceleration of other earthquakes. The time since the most recent earthquakes in the Maqin and Maqu sections is approaching or has exceeded the recurrence time of each segment's earthquakes. Furthermore, the stress of the Maqin and Maqu sections was amplified by the 2008 Wenchuan M_S 8.0 earthquake. Consequently, the middle EKFZ presents a higher earthquake risk [15].

The research area falls within a transition zone that exhibits characteristics of both arid and semi-arid climates, accompanied by cold alpine conditions [29]. The yearly mean temperature hovers around −3.7 °C to −7.7 °C [30], and the annual precipitation amounts to ~250 mm, concentrated mainly in summer. The region experiences high evaporation rates and a dry climate. Surface water sources include atmospheric precipitation, glacial meltwater, and lakes. [30,31]. The topography of the study area slopes downward from the higher northeast to the lower southwest. Previous studies have indicated that the lithology near the fault zone primarily consists of Carboniferous limestone, Indo-Chinese epoch porphyritic biotite granites, along with Permian, Triassic, and Cretaceous feldspar-quartz sandstone [32]. The extensive exposure of intrusive rocks such as granite is related to magmatic activity dating back to the Permian and Triassic periods.

The magmatic history of the central-eastern part of the Eastern Kunlun Fault Zone spans the period from the Paleozoic to the Cenozoic. In the Paleozoic to Early Mesozoic, magmatism was possibly linked to island arc formation and oceanic spreading, intensifying with the closure of the Paleo-Tethys Ocean. The Mesozoic was marked by significant intrusions, especially granites and metallic minerals during the Triassic to Jurassic periods, driven by the India–Eurasia interaction. The Late Mesozoic to Cenozoic saw a continued uplift of the Tibetan Plateau, with magmatic activities related to crustal stretching and mantle upwelling. The intrusion and uplift of granite to the Earth's surface contribute to an increase in the geothermal gradient to some extent in the study area [33,34]. Recent magmatic activities and geothermal phenomena in the Quaternary, especially the Holocene, suggest ongoing sub-crustal processes [35,36].

In the Eastern Kunlun Fault Zone, intense tectonic movements, especially the processes of faulting and uplifting, have resulted in the development of fractures and the enhanced connectivity of fissures. Simultaneously, the primary and secondary fault systems in the eastern part of the Eastern Kunlun Fault Zone have a decisive impact on the flow and distribution of groundwater. The tectonic activity in the region and the thermal properties of intrusive rocks may promote the formation of hydrothermal systems. Geothermal fluids are typically heated in deeper geological settings and then ascend to shallower strata or the surface through fracture systems.

Preprints.org (www.preprints.org) | NOT PEER-REVIEWED | Posted: 19 March 2024 doi:10.20944/preprints202403.1101.v1

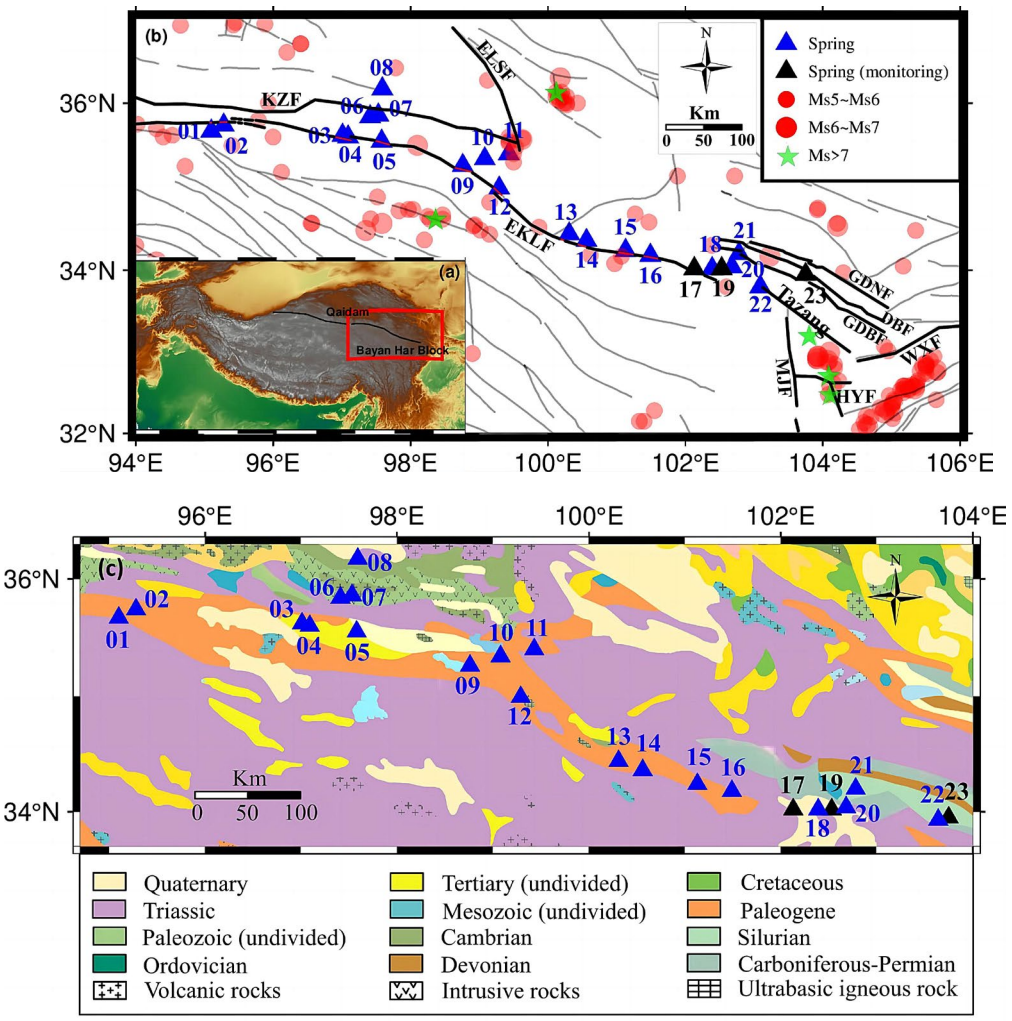

Figure 1. (**a**) Macro-regional map [37]. (**b**) Active structure map with locations of sampling sites in the mid-eastern part of the Kunlun Mountain Fault. KZF: Kunzhong Fault; EKF: Eastern Kunlun Fault; ELSF: Eelashan Fault; JGF: Jungong Fault; HYF: Huya Fault; MJF: Minjiang Fault; WXF: Weixi Fault; GDNF: Guanggaishan–Dieshannanmi Fault; GDBF: Guanggaishan–Dieshanbeimi Fault; circle: earthquake; black square frame: sampling area; triangles: sampling sites [38]. (**c**) Geological map with sampling sites of the study area (black line): the sites indicated with black triangles were sampled once, while the red triangles represent the long-term monitoring stations with a sampling frequency of 3 days.

Table 1. The fault slip rate of the EKF [15].

Segment	Horizontal Slip Rate (mm/a)	Vertical Slip Rate (mm/a)
Tuosuohu	11.2 ± 1.2	1.2 ± 0.2
Maqin	9.3 ± 2.0	0.7 ± 0.1
Xigongzhou intersection zone	7.4 ± 1.0	1.2 ± 0.1
Maqu	4.9 ± 1.3	0.3

3. Sampling and Methods

A total of 23 varied-temperature springs along the EKF were sampled for groundwater analysis from May to July 2021 (see Figure 1). Two methods, a census and detailed surveys, were employed for sample analysis. In the detailed survey stage, three springs were selected for continuous monitoring, with varied-temperature water samples collected every three days for geochemical

Preprints.org (www.preprints.org) | NOT PEER-REVIEWED | Posted: 19 March 2024 doi:10.20944/preprints202403.1101.v1

analysis. A total of 609 water samples were collected, with 587 obtained from the three continuously monitored springs. In the southeastern part of the Eastern Kunlun Fault Zone, our study suggests that the springs, including the three continuously monitored thermal springs, are primarily replenished by fissure water and underground runoff from the northwestern mountains, manifesting as descending springs. The overlying strata predominantly consist of Permian and Triassic carbonate rocks. It is important to note that our inference regarding the predominantly descending nature of the springs is based on the observed topographical decline from west to east in the study area, as well as on the research conducted by Lu Chang et al. in this location. However, due to the current lack of comprehensive hydrogeological data, we cannot completely rule out the possibility of ascending springs that may originate from deeper underground [39].

During sampling, the sampler wore rubber gloves and rinsed the sampling polyethylene terephthalate (PET) bottle (50 mL) three times with spring water. When collecting samples, we ensured that the bottle was fully immersed in water and tightly sealed to prevent air from entering. Additionally, we recorded the weather, sampling time, odor, sampling location, and exposed lithology. Finally, the collected samples were promptly transported to the laboratory. These samples were preserved in 50 mL PET containers and stored at a temperature of 4 °C.

In the laboratory, various parameters were analyzed, including conductivity, pH, dissolved oxygen, cationic concentration (Na^+, K^+, Mg^{2+}, Ca^{2+}, etc.), anion concentration (NO_3^-, SO_4^{2-}, Br^-, CO_3^{2-}, HCO_3^-, etc.), isotopes (hydrogen, oxygen, and strontium) and other indicators. The pH, conductivity, and dissolved oxygen data were collected using a multiparameter probe. Water temperature was measured using a digital thermometer with a precision of 0.1 °C during sample collection. The HCO_3^- and CO_3^{2-} contents were determined using chemical titration with a ZDJ–100 potentiometric titrator with a solution of 1% phenolphthalein, 0.1% methyl orange, and 0.05 mol/L HCl. (Place 5ml of water sample in a beaker, and add two drops of phenolphthalein. If the solution does not change color, add another two drops of methyl orange. Then, using a 1ml dropper, add hydrochloric acid until the solution becomes colorless. The amount of hydrochloric acid used represents the concentration of carbon dioxide. If the solution changes color after adding two drops of phenolphthalein, add hydrochloric acid with a 1ml dropper until the solution becomes colorless. Then, add two drops of methyl orange and record the concentration of carbonate dioxide) For cation (Ca^{2+}, K^+, Mg^{2+}, and Na^+) and anion (NO_3^-, CO_3^{2-}, HCO_3^-, Br^-, and SO_4^{2-}) concentration estimation, water samples were diluted tenfold and transferred to 2 mL PET bottles. The concentrations were measured using a Dionex ICS-900 ion chromatograph and AS 40 automatic sampler at the Key Laboratory of Earthquake Prediction of China Earthquake Administration. The reproducibility of the measurements was within ±2%, and the detection limit was 0.01 mg/L. Data management and analysis were performed using a Dionex ICS-900 ion chromatograph and an AS40 automatic sampler with a reproducibility of ±5% or less and a detection limit of 0.01 mg/L at the Earthquake Forecasting Key Lab of China Earthquake Administration [20]. The reliability of the data was evaluated using ion balance (*ib*) equations.

$$ib(\%) = \frac{\sum cation - \sum anion}{\sum cation + \sum anion} \times 100\% \quad (1)$$

Trace elements were analyzed at the Test Center of the Research Institute of Uranium Geology using Element XR ICP-MS (Thermo Fisher, Bremen, Germany) .The SiO_2 concentration was obtained by multiplying the measured silicon concentration using the 5300DV Inductively Coupled Plasma Emission Spectrometer by a factor of 2.13. The hydrogen and oxygen isotopes were analyzed using a Finnigan MAT253 mass spectrometer at the Earthquake Forecasting Key Lab of China Earthquake Administration. The TC/EA method was employed, with V-SMOW serving as the standard. The analytical accuracy for the samples was within the range of $-1‰ < \delta D < 1‰$ for hydrogen isotopes and $-0.2‰ < \delta^{18}O < 0.2‰$ for oxygen isotopes. Additionally, the Sr isotope analysis was conducted using the Phoenix Thermal Surface Ionization Mass Spectrometer, with an error of 2σ.

Preprints.org (www.preprints.org) | NOT PEER-REVIEWED | Posted: 19 March 2024 doi:10.20944/preprints202403.1101.v1

4. Results

4.1. Major and Trace Element Concentrations in Water Samples

Table 2 presents the concentrations of significant elements, while Table 3 provides the concentrations of trace elements. The ion balance equations indicated that the measurement error of ions was less than 5%, confirming the usefulness of the data [40,41].

Based on the data in Table 2, the recorded temperatures of the varied-temperature springs ranged from 2.2 °C to 60.4 °C, with the majority being cool springs. Among these springs, 18 have been identified as cold springs, with temperatures ranging from 2.2°C to 22.2°C and an average temperature of 9.3°C. However, this is still significantly higher than the local average temperature of -3.7°C. Additionally, there were two low-temperature springs (25 °C < T < 40 °C) and three medium-temperature springs (40 °C < T < 75 °C), with temperature ranges of 25.9–28 °C and 44.2–60.4 °C, respectively. The average temperature for the low-temperature springs was 26.95 °C, while the mean value for the medium-temperature springs was 51.2 °C. The spring numbered EKF 11 exhibited the highest temperature, reaching 60.4 °C. It is speculated that the variation in temperature is primarily attributed to differences in circulation depth and the mixing of springs with other water bodies to some extent during their ascent. [42].

Table 2 also displays a significant variation in electric conductivity and TDS (total dissolved solids). The electric conductivity ranged from 349.8 to 4577 μs/cm. The lowest conductivity was recorded at EKF 14, while the highest conductivity was observed at EKF 9, which was 13 times higher than the lowest value. The TDS values ranged from 332.12 to 3753.51 mg/L. Interestingly, the eastern varied-temperature springs in the study area exhibited lower TDS and electric conductivity values. The pH values ranged from 7.34 to 8.60, with an average value of 8, indicating the alkaline nature of these springs.

Regarding the analysis of chemical element concentrations, a piper plot was created in subsequent chapters. From Table 2, it is evident that the main cations are Ca^{2+}, Na^{+}, and Mg^{2+}, and the main anion is $HCO3^{-}$. However, notable levels of SO_4^{2-} and CO_3^{2-} were also observed in some springs. In addition to the major elements, Table 3 summarizes the results of the trace element analysis. It is evident from Table 3 that elements such as B, Sr, and Li exhibit significantly higher concentrations compared to other trace elements. Furthermore, the water samples contain various minor elements, as observed in the analysis.

4.2. Isotopes

The isotopes' characteristics are illustrated in Table 2. The stable hydrogen isotopic ratios (δD) of the water samples range from -107.3‰ to -67.2‰, while the stable oxygen isotopic ratios ($\delta^{18}O$) range from -14.4‰ to -6.9‰. Additionally, the 87Sr/86Sr ratio ranges from 0.707827 to 0.713388.

Preprints.org (www.preprints.org) | NOT PEER-REVIEWED | Posted: 19 March 2024 doi:10.20944/preprints202403.1101.v1

Table 2. The composition of spring water ions, hydrochemistry type, and $^{87}Sr/^{86}Sr$ ratios. (Water temperature was measured using a digital thermometer with a precision of 0.1 °C during sample collection.).

No.	T/°C	Latitude/°	Altitude/°	pH	Conductivity /μs·cm^{-1}	TDS /g·L^{-1}	Na^+ /mg·L^{-1}	K^+ /mg·L^{-1}	Mg^{2+} /mg·L^{-1}	Ca^{2+} /mg·L^{-1}	Cl^- /mg·L^{-1}	NO_3^- /mg·L^{-1}	SO_4^{2-} /mg·L^{-1}	CO_3^{2-} /mg·L^{-1}	HCO_3^- /mg·L^{-1}	Si /mg·L^{-1}	$^{87}Sr/^{86}Sr$	$\delta^{18}O$/‰	Hydrochemical Type
EKF 1	2.2	95.10	35.67	7.9	1538	1.21	104.4	2.7	115.2	104.3	154.2	14.3	492.1	25.2	194.4	2.17	0.710500	-12.3	Mg-SO_4-HCO_3
EKF 2	22.2	95.28	35.74	8.2	1205	0.82	145.2	4.6	56.2	50.9	197.9	6.8	155.4	32.0	172.9	0.46	0.710500	-9.1	Na-Mg-HCO_3-Cl
EKF 3	20.0	97.01	35.62	8.6	2298	1.52	331.5	6.3	92.8	68.0	666.3	0.0	186.0	54.4	116.9	0.84	0.711000	-6.9	Na-Cl
EKF 4	6.2	97.09	35.60	7.6	721	0.51	53.6	2.6	20.2	82.0	103.9	5.5	70.4	0.0	176.4	2.86	0.711334	-10.8	Ca-Na-HCO_3
EKF 5	15.3	97.58	35.55	7.7	2114	1.68	304.5	11.6	66.1	130.0	366.6	9.3	240.3	36.7	519.5	9.67	0.708655	-11.1	Na-HCO_3
EKF 6	4.1	97.41	35.84	8.0	745	0.54	63.9	2.4	17.8	86.4	84.1	6.3	102.6	0.0	176.4	1.82	0.713388	-10.2	Ca-Na-HCO_3
EKF 7	7.0	97.53	35.86	7.8	2143	1.58	248.3	7.7	55.1	184.9	487.8	43.1	276.0	0.0	278.8	2.8	0.712260	-11	Na-Ca-Cl-HCO_3
EKF 8	25.9	97.59	36.17	8.6	915	0.64	108.2	5.6	39.0	49.0	135.1	5.9	96.8	51.7	144.6	4.75	0.711116	-7.8	Na-HCO_3
EKF 9	14.5	98.76	35.26	8.1	4577	3.75	673.1	14.6	303.8	76.4	1219.0	11.1	891.6	71.4	492.5	3.64	0.710054	-7.7	Na-Mg-Cl
EKF 10	9.3	99.08	35.34	7.8	3690	3.10	521.8	13.5	172.3	195.9	932.8	22.6	901.7	0.0	342.4	3.65	0.713214	-12.7	Na-Cl-SO_4
EKF 11	60.4	99.43	35.40	7.8	1624	1.21	309.6	20.9	4.8	57.5	181.1	11.0	456.3	0.0	172.9	34.60	0.712407	-10.8	Na-SO_4
EKF 12	4.5	99.29	34.99	8.1	866	0.78	18.3	2.1	44.1	145.4	31.1	5.4	207.5	54.5	273.0	2.73	0.708718	-12.1	Ca-Mg-HCO_3
EKF 13	10.0	100.31	34.44	8.1	695	0.61	24.8	1.7	37.7	100.7	8.7	1.1	74.6	38.2	325.1	2.93	0.715374	-10.9	Ca-Mg-HCO_3
EKF 14	4.5	100.56	34.36	8.2	350	0.34	5.5	1.6	13.6	65.7	0.5	4.8	6.6	0.0	240.1	3.96	0.712455	-10.8	Ca-HCO_3
EKF 15	6.5	101.13	34.24	7.9	464	0.52	7.4	1.2	20.2	100.9	0.4	2.4	14.3	0.0	369.2	4.03	0.718426	-10.5	Ca-HCO_3
EKF 16	6.5	101.49	34.18	7.8	470	0.57	6.5	1.5	9.8	124.3	2.2	8.6	5.2	0.0	408.1	5.85	0.707998	-11.5	Ca-HCO_3
EKF 17	9.0	102.27	34.02	8.0	460	0.47	5.2	0.8	19.9	95.5	0.5	4.0	4.8	0.0	335.8	3.13	0.708728	-12.4	Ca-HCO_3
EKF 18	4.5	102.39	34.02	7.9	509	0.55	9.4	1.3	26.8	100.9	1.1	0.0	0.9	0.0	412.8	4.34	0.715199	-13.7	Ca-HCO_3
EKF 19	12.0	102.46	34.02	8.0	446	0.40	3.5	0.8	21.4	76.3	0.4	0.6	10.0	18.7	272.4	4.19	0.708887	-13.7	Ca-Mg-HCO_3
EKF 20	28.0	102.68	34.04	8.0	441	0.43	4.0	1.4	17.0	86.7	0.3	0.7	10.0	19.5	293.5	6.40	0.711761	-13	Ca-HCO_3
EKF 21	49.0	102.78	34.20	7.6	1201	1.38	44.6	7.0	66.5	226.4	1.5	0.4	229.7	0.0	799.8	14.52	0.708718	-14.4	Ca-Mg-HCO_3
EKF 22	—	103.63	33.93	8.2	392	0.33	4.2	1.3	25.8	53.8	1.8	4.3	8.2	0.0	232.6	—	—	—	—
EKF 23	44.2	103.69	33.95	7.3	1366	1.29	77.9	5.3	66.8	184.8	22.9	0.0	451.4	0.0	477.3	10.40	0.707827	-12.6	Ca-Mg-HCO_3

Preprints.org (www.preprints.org) | NOT PEER-REVIEWED | Posted: 19 March 2024 doi:10.20944/preprints202403.1101.v1

Table 3. Trace elements of spring water samples.

No.	Ag /μg·L^{-1}	Al /μg·L^{-1}	Ba /μg·L^{-1}	Be /μg·L^{-1}	Cd /μg·L^{-1}	Co /μg·L^{-1}	Cr /μg·L^{-1}	Cu /μg·L^{-1}	Fe /μg·L^{-1}	Li /μg·L^{-1}	Mn /μg·L^{-1}	B /μg·L^{-1}
EKF1	0.06	144	34.1	0.084	0.03	0.391	4.47	2.67	338	22.3	10.9	139
EKF2	0.002	75.7	42.8	0.068	0.021	0.388	3.65	3.56	190	66.6	20.3	1990
EKF3	0.018	25.3	53.6	0.109	0.012	0.359	3.68	6.66	78.7	84.4	4.23	534
EKF4	0.003	38.4	68.9	0.052	0.008	0.135	1.85	2.38	79.5	17.7	2.97	137
EKF5	0.134	276	168	0.128	0.025	0.641	3.79	7.45	384	192	121	1032
EKF6	<0.002	221	91.6	0.031	0.019	0.27	3.68	4.09	467	11.3	11.4	118
EKF7	0.007	29.4	71.9	0.024	0.025	0.425	6.2	5.87	61.4	21.8	1.93	363
EKF8	0.003	28.3	27.5	0.059	0.011	0.161	3.78	2.3	214	40.2	14.8	360
EKF9	0.018	83.1	61.6	0.087	0.12	0.904	10.6	111	509	187	80.7	1190
EKF10	0.015	20.5	27.2	0.097	0.019	0.55	8.02	9.27	172	106	339	702
EKF11	0.014	21.8	27.8	0.267	0.015	0.094	3.74	4.99	23.1	1168	1.49	1768
EKF12	0.003	14.6	96.8	3.62	0.014	0.3	1.04	17.5	14	1145	9.67	2029
EKF13	<0.002	6.47	66	1.54	<0.002	0.295	0.867	21.1	62	1324	117	1483
EKF14	0.003	42.3	50.5	23.7	0.029	0.353	1.48	23.5	51	795	137	4.17
EKF15	<0.002	13.1	8.32	0.131	0.018	0.057	0.442	13.7	45	232	9.79	215
EKF16	<0.002	5.71	51.3	0.929	0.033	0.142	0.532	15.8	45	1172	32	852
EKF17	0.005	36.9	33.2	0.725	0.038	1.52	0.635	18.9	39	200	32.4	8.73
EKF18	0.004	6.09	85.5	1.18	0.066	0.223	0.716	15.4	12	573	488	70.7
EKF19	0.003	10.9	107	6.22	0.041	0.231	1.22	18.8	137	1631	75.5	2385
EKF20	0.002	6.08	53.2	0.886	0.008	0.412	3.57	19.7	27	2047	34.1	18,330
EKF21	0.003	2.03	29.9	0.683	0.049	1.6	1.65	25.8	23	217	139	614
EKF23	0.006	2.79	44.3	0.223	0.042	0.238	1.64	1.54	63.7	135	11.6	517

Preprints.org (www.preprints.org) | NOT PEER-REVIEWED | Posted: 19 March 2024 doi:10.20944/preprints202403.1101.v1

Table 3. Cont.

No.	Mo /mg·L^{-1}	Ni /mg·L^{-1}	Pb /µg·L^{-1}	Sb /µg·L^{-1}	Sn /µg·L^{-1}	Sr /µg·L^{-1}	Th /µg·L^{-1}	Ti /µg·L^{-1}	Tl /µg·L^{-1}	U /µg·L^{-1}	V /µg·L^{-1}	Zn /µg·L^{-1}
EKF1	0.305	3.95	0.918	0.028	0.017	1394	0.051	3.96	0.005	4.66	5.76	4.2
EKF2	1.52	3.42	0.61	0.353	0.086	896	0.014	3.01	0.016	3.95	6.82	6.28
EKF3	3.02	3.83	0.445	0.26	0.093	1385	0.007	1.79	0.002	6.67	23.4	3.76
EKF4	0.788	3.05	0.355	0.046	0.097	769	0.025	2.7	<0.002	2.48	5.02	19.9
EKF5	2.15	11	0.795	0.156	0.1	8461	0.044	9.48	0.016	8.36	14.8	12.9
EKF6	2.21	4.44	0.438	0.081	0.149	478	0.085	18.2	0.003	22.3	5.35	4.34
EKF7	4.72	6.49	0.678	0.135	0.087	1399	0.017	3.81	0.009	40.8	16.5	9.39
EKF8	2.74	1.7	0.328	0.128	0.042	805	0.012	2.94	0.008	4.71	6.63	2.57
EKF9	1.08	272	1.91	0.354	1.14	1856	0.024	4.55	0.02	6.7	39	322
EKF10	1.18	7.26	0.522	0.135	0.057	2900	0.008	2.99	0.013	16	30.6	5.41
EKF11	1.97	1.87	0.584	1.05	0.06	812	0.009	11.8	0.148	1.47	12.9	4.81
EKF12	1.13	5.85	0.141	14.1	0.369	988	<0.002	10.5	1.21	6.74	6.35	80.2
EKF13	0.255	6.49	0.797	12.2	0.525	975	<0.002	8.19	0.201	0.139	0.554	136
EKF14	5.24	5.01	0.169	6.04	0.426	2396	0.003	9.58	0.271	0.259	1.04	83.9
EKF15	1.74	1.31	0.131	0.861	0.425	127	<0.002	6.02	0.01	0.529	0.402	50
EKF16	15	4.28	1.06	2.53	0.588	881	<0.002	11.4	0.525	0.078	0.605	62.9
EKF17	1.66	33.2	0.15	19.7	0.356	12,534	0.002	4.87	0.053	0.386	0.288	106
EKF18	0.168	4.08	0.147	0.241	0.495	254	<0.002	12	0.03	0.159	0.725	79.7
EKF19	0.538	4.68	0.16	4.84	0.536	1364	0.009	11.8	1.06	0.203	0.97	75.1
EKF20	0.226	8.06	0.221	51.9	0.556	2754	<0.002	6.29	0.01	0.139	1.98	74.2
EKF21	1.04	23.5	0.117	0.464	0.434	9662	<0.002	3.77	0.087	0.405	10.5	218
EKF23	1.29	7.28	0.251	0.033	0.097	14,309	0.018	5.02	0.009	4.55	0.306	18

Preprints.org (www.preprints.org) | NOT PEER-REVIEWED | Posted: 19 March 2024 doi:10.20944/preprints202403.1101.v1

5. Discussion

5.1. Water Origin and δD, $\delta^{18}O$

Multiple studies have demonstrated that hydrogen and oxygen isotope values exhibit significant differences in various water sources, such as geothermal water, atmospheric precipitation, and magmatic water. This characteristic allows for the determination of the source of geothermal water [43]. From Figure 2, it can be observed that the springs in the region are primarily concentrated around the atmospheric precipitation line, suggesting that their origin is linked to atmospheric precipitation. The local atmospheric precipitation line is located in the bottom-right part of the precipitation line because the Eastern Kunlun region is different from the ocean and has a dry climate. Much of the atmospheric precipitation results from local water vapor evaporation. During evaporation, the proportion of heavy isotopes increases, resulting in an elevated hydrogen and oxygen isotope ratio [44]. The graph depicting the relationship between δD and $\delta^{18}O$ illustrates higher isotopic values in the west compared to the east. This pattern likely results from the higher slip rates and more intense tectonic activity in the western region, leading to increased contact between water and rocks, facilitating the incorporation of more hydrogen and oxygen isotopes into the water. Among all samples, it is noteworthy that springs Nos. 3, 5, 8, 9, and 11 exhibit an obvious positive $\delta^{18}O$ drift. Existing research by Pang et al., 2017, and Li et al., 2017, indicates that a positive $\delta^{18}O$ shift suggests intensive water–rock interactions. These five springs are located near or at fault zones, where the fault cutting is deep, and the duration of water–rock interactions is prolonged. The occurrence of this phenomenon can be attributed to the strong reactions between the water and rock, resulting in the continuous enrichment of $\delta^{18}O$ isotopes in the varied-temperature spring water upon contact with the rock [45–47]. Springs Nos. 1, 7, and 23, situated to the left of the atmospheric precipitation line, display a negative $\delta^{18}O$ shift, which can be attributed to the blend of diverse water sources. Springs Nos. 1 and 7 are situated near a snow-capped mountain and may incorporate a significant amount of snowmelt water. Spring No. 23 is located near a fault zone, potentially being replenished by deep water within the fault zone [48]. A well-documented relationship known as the elevation effect exists between altitude and $\delta^{18}O$. Based on this relationship, the recharge elevation of groundwater can be determined [49]. By analyzing the $\delta^{18}O$ data of the water samples (see Table 2) using the formula $\delta^{18}O = -0.002ALT - 6.327$, the groundwater recharge elevation is found to range from 0.3 km to 4 km in the study area [50]. Excluding hot spring sites with intense water–rock reactions and others where mixing may occur, the recharge elevation for groundwater in the Tuosuo Lake section ranges from 1.4 to 3.2 km. For the Maqin–Maqu section, the groundwater recharge elevation is between 2.1 and 2.6 km, and for the Tazang section, it ranges from 3.0 to 4.0 km.

Preprints.org (www.preprints.org) | NOT PEER-REVIEWED | Posted: 19 March 2024 doi:10.20944/preprints202403.1101.v1

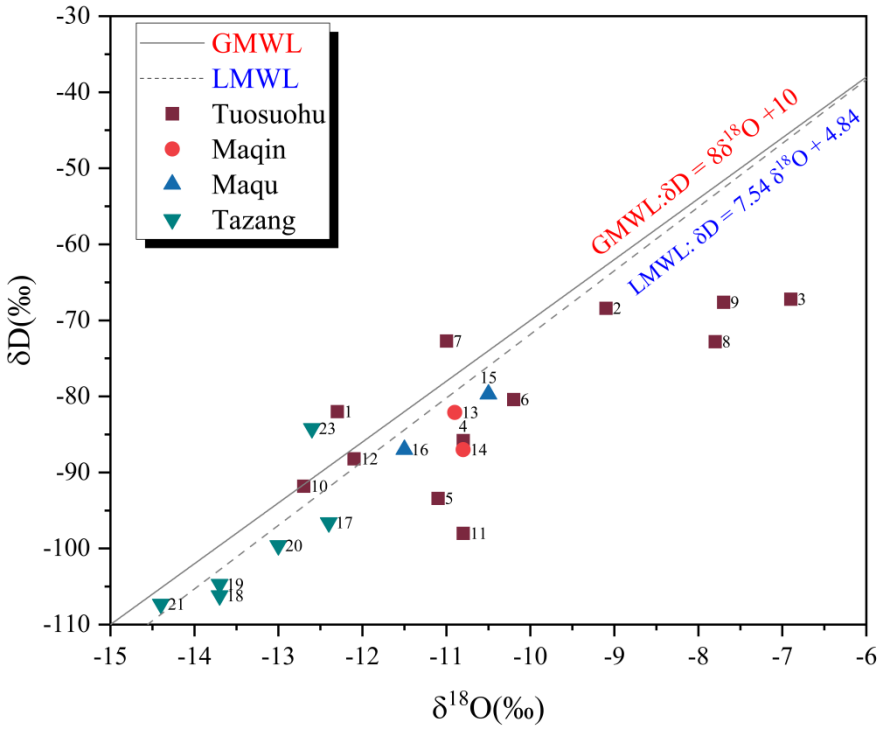

Figure 2. Graph of the relationship between δD and $\delta^{18}O$. GMWL: δD = 8$\delta^{18}O$ +10 [51]; LMWL: δD = 7.54 $\delta^{18}O$ + 4.84 [52].

5.2. Sr Isotope

The ^{87}Sr isotope can be obtained from the β-decay of ^{87}Rb. It is commonly found in minerals that are rich in calcium and potassium [53]. By analyzing the chemical makeup of spring water (see Table 2), it was observed that Ca^{2+} and Mg^{2+} are widely present in the region, suggesting the presence of a significant amount of Sr. Previous research by Shand (2009) showed that $^{87}Sr/^{86}Sr$ does not participate in hydration reactions and has high mobility [54].

Exploiting the characteristics of Sr, we can use both Sr concentrations and $^{87}Sr/^{86}Sr$ ratios to determine the source of various chemical components in water samples and identify whether groundwater is mixed. To facilitate this analysis, a diagram depicting the correlation between Sr concentrations and $^{87}Sr/^{86}Sr$ ratios was created (see Figure 3). In this study, we observed that the $^{87}Sr/^{86}Sr$ ratio in water samples primarily ranged from 0.708 to 0.716. The occurrence of this range can be attributed to the widespread distribution of carbonates, silicates, and surface waters in the study area. The formation of this phenomenon is closely related to the deep circulation process of atmospheric precipitation in the local thermal fluid system, during which water interacted with strontium-rich crustal rocks.

Springs Nos. 1, 2, 3, 4, 8, 12, 15, 16, and 21 exposed near rivers and sinkholes, belonging to the Quaternary system as descending springs with potential replenishment from surrounding shallow waters. Therefore, they are situated close to the river water depicted in the map. On the other hand, the Tuosuohu, Maqin, and Maqu sections contain high amounts of silicates and low amounts of carbonates. As a result, in the remaining hot springs such as those in Tuosuohu and Maqin, the $^{87}Sr/^{86}Sr$ ratios predominantly range between 0.711 (river water) and 0.716 (silicate), as observed in springs numbered 6, 7, 10, 11, and 13. Notably, the Sr concentration of the Tazang water samples is concentrated between 0.708 and 0.711. The highest Sr concentration is observed in the Tazang section, which can be attributed to groundwater flowing through a significant amount of limestone in that area. Additionally, the presence of multiple faults, such as GDNF and GDBF, in this section increases the contact area between groundwater and rock.

Preprints.org (www.preprints.org) | NOT PEER-REVIEWED | Posted: 19 March 2024 doi:10.20944/preprints202403.1101.v1

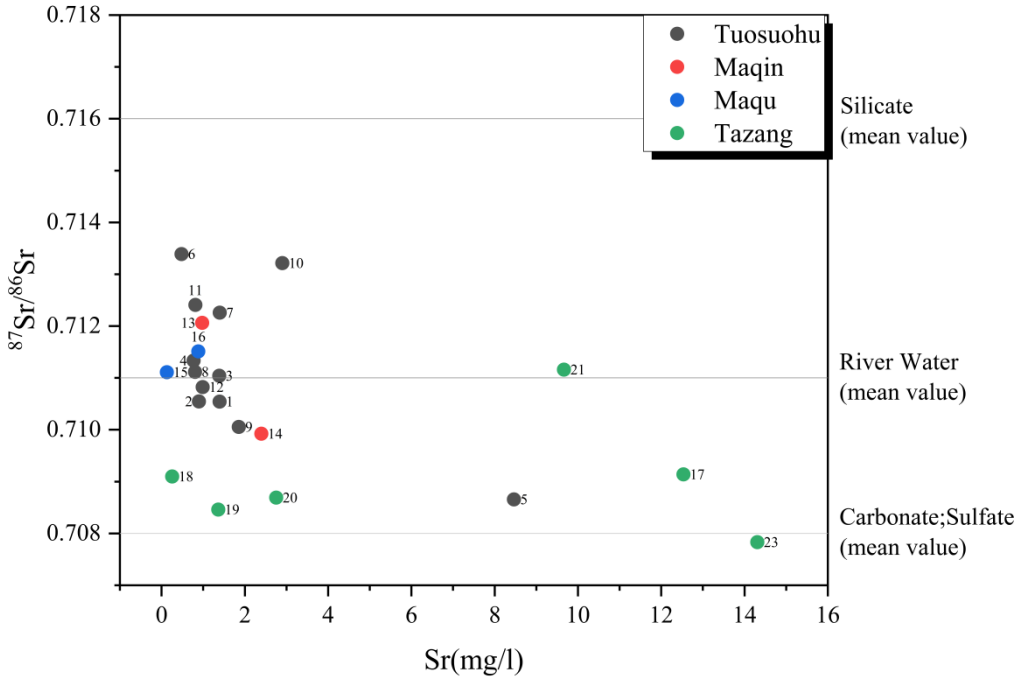

Figure 3. Relationship between the Sr concentration and $^{87}Sr/^{86}Sr$ ratio.

5.3. Major Elements

A Piper diagram was constructed (see Figure 4) to determine the water chemistry types for each sampling point, which are recorded in Table 2. Based on the water chemistry types identified, it can be observed that there are 11 distinct types of water chemistry in the study area, namely, Na-Mg-HCO_3-Cl, Mg-SO_4-HCO_3, Na-Cl, Na-HCO_3, Ca-Na-HCO_3, Na-Ca-Cl-HCO_3, Na-Cl-SO_4, Na-SO_4, Na-Mg-Cl, Ca-Mg-HCO_3, and Ca-HCO_3. In the Tuosuohu area, the main ions are Na^+, Ca^{2+}, Cl^-, and HCO_3^-. Meanwhile, in the Maqin, Maqu, and Tazang sections, the dominant ions are Mg^{2+}, Ca^{2+}, and HCO_3^-. The Ca-HCO_3-type water is characteristic of leaching water in sedimentary rock areas and is primarily concentrated in the Maqin, Maqu, and Tazang sections. This can be attributed to the abundance of limestone in these areas. Limestone is composed of carbonate rocks, including calcite and dolomite, which are rich in $CaCO_3$ and $MgCO_3$. As groundwater flows through the limestone, it dissolves the Ca^{2+}, Mg^{2+}, and HCO_3^- present in the rocks.

The Ca/Mg values in the research region range from 0.25 to 12.67, with an average of 3.71. A Ca/Mg value greater than 1 indicates the high solubility of groundwater in limestone. The Na/K values in the Tuosuohu segment range from 8.85 to 52.86, with an average of 29.66, while the Na/Ca values in the same segment range from 0.65 to 8.81, with an average of 2.99. In the Maqin, Maqu, and Tazang segments, the Na/K values range from 2.87 to 14.84, with an average of 6.707, and the Na/Ca ratios vary between 0.05 and 0.42, with an average of 0.13. The relatively low values of Na/K and Na/Ca, with higher values in the northwestern mountainous area compared to the southeastern section, may suggest that the spring water originates from a descent spring fed by an aquifer in front of a mountain in the Maqin, Maqu, and Tazang regions [55]. The diversity in total ionic salinity (TIS) is noticeable in the varied-temperature spring samples, as evident from the correlation plot of SO_4^{2-} + HCO_3^- vs. Cl^- (see Figure 5). The majority of the spring waters analyzed have TIS values below 30 meq/kg. The comprehensive analysis of major elements indicates that the varied-temperature springs possess complex compositions (see Table 2).

To assess the balance of water–rock reactions, the Na–K–Mg triangle diagram was employed (see Figure 6) [56]. In this study, all samples are located along the $Mg^{1/2}$ endmember, indicating an insufficient reaction between groundwater and the surrounding rock. This observation supports the hypothesis that the fracture connectivity is strong and the water circulation speed is fast, leading to inadequate water–rock reactions and the mixing of thermal groundwater with cold water during ascent. Hot spring No. 11 is closer to partially balanced water, which can be attributed to its location

Preprints.org (www.preprints.org) | NOT PEER-REVIEWED | Posted: 19 March 2024 doi:10.20944/preprints202403.1101.v1

near the fault intersection zone (ELSF and KZF), where the fault is deeper, resulting in a longer water–rock reaction time and a higher dissolution of rock components in the water.

The mineral saturation index (SI) of thermal springs provides insights into the thermodynamic behavior of minerals and the equilibrium process between water and rock. This index helps to predict the types of minerals that are deposited during the circulation of varied-temperature water. Typically, an SI value ranging from 0 to 0.2 indicates that the mineral is in an equilibrium state. A positive SI indicates supersaturation, while a negative SI suggests the continued dissolution of the mineral. In this study, the mineral saturation index (SI) was determined using PHREEQC software (see Figure 7). It is evident that all samples of varied-temperature spring water exhibit supersaturation (SI > 0) with respect to hematite and goethite. This indicates that these minerals are abundant in the water and continuously precipitate as the hot water rises. On the other hand, gibbsite and fluorite exhibit equilibrium conditions (SI ≈ 0). Most other minerals are in an unsaturated state (SI < 0). This can be attributed to the low mineral content, short reaction time between water and rock, and inherent characteristics of the minerals themselves. The saturation index with respect to hausmannite and pyrolusite shows significant variation among the varied-temperature spring waters, reflecting differences in the distribution characteristics of surrounding rocks to some extent.

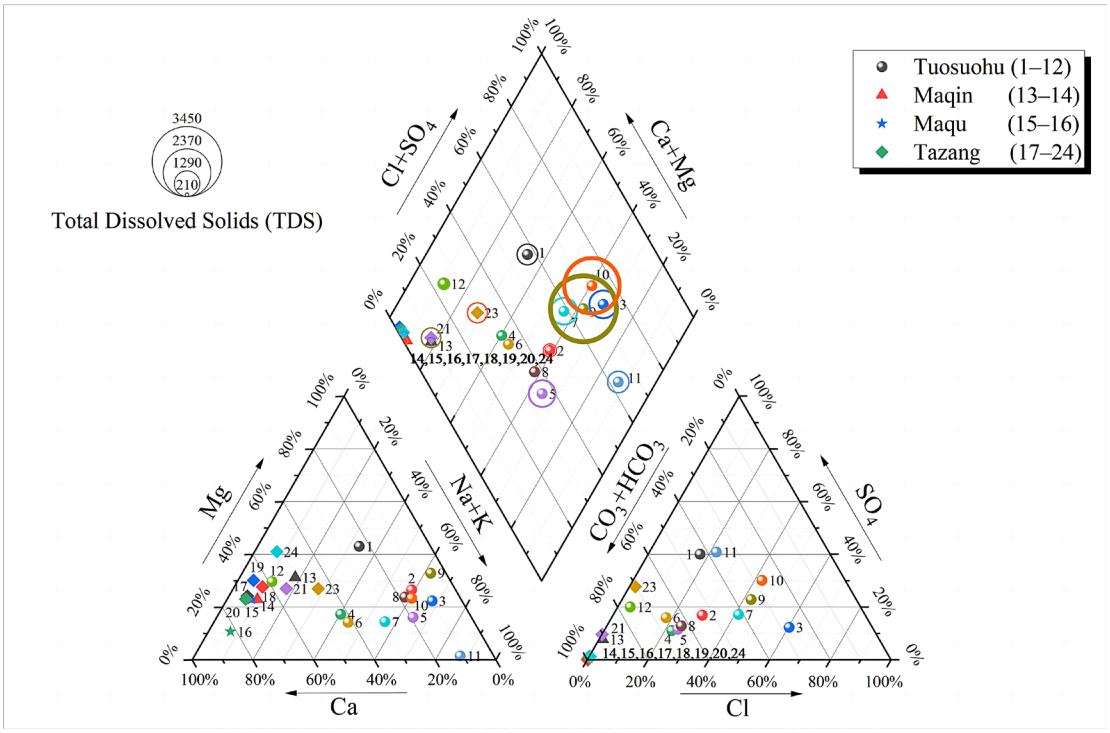

Figure 4. Piper diagram.

Preprints.org (www.preprints.org) | NOT PEER-REVIEWED | Posted: 19 March 2024 doi:10.20944/preprints202403.1101.v1

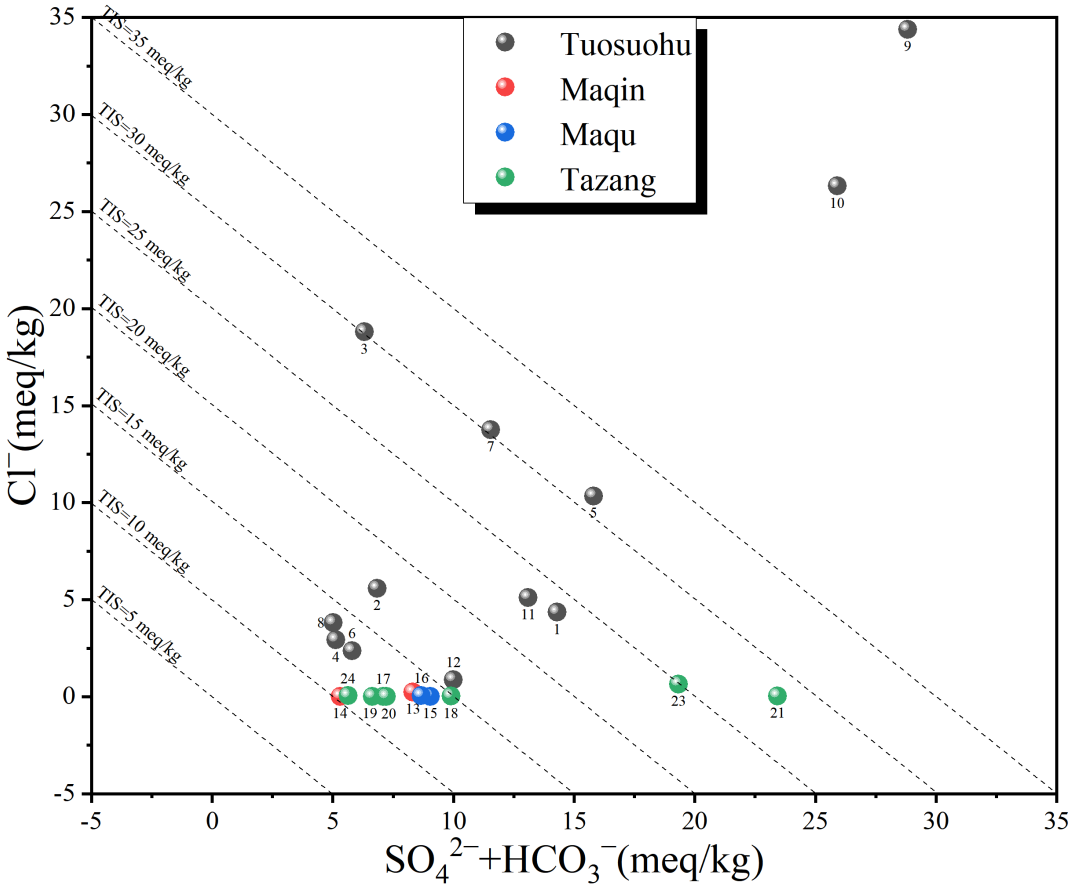

Figure 5. The correlation plot illustrates the relationship between SO_4^{2-} + HCO_3^- and Cl^- in the varied-temperature springs of the EKF, while also displaying isolines of total ionic salinity (TIS) for reference.

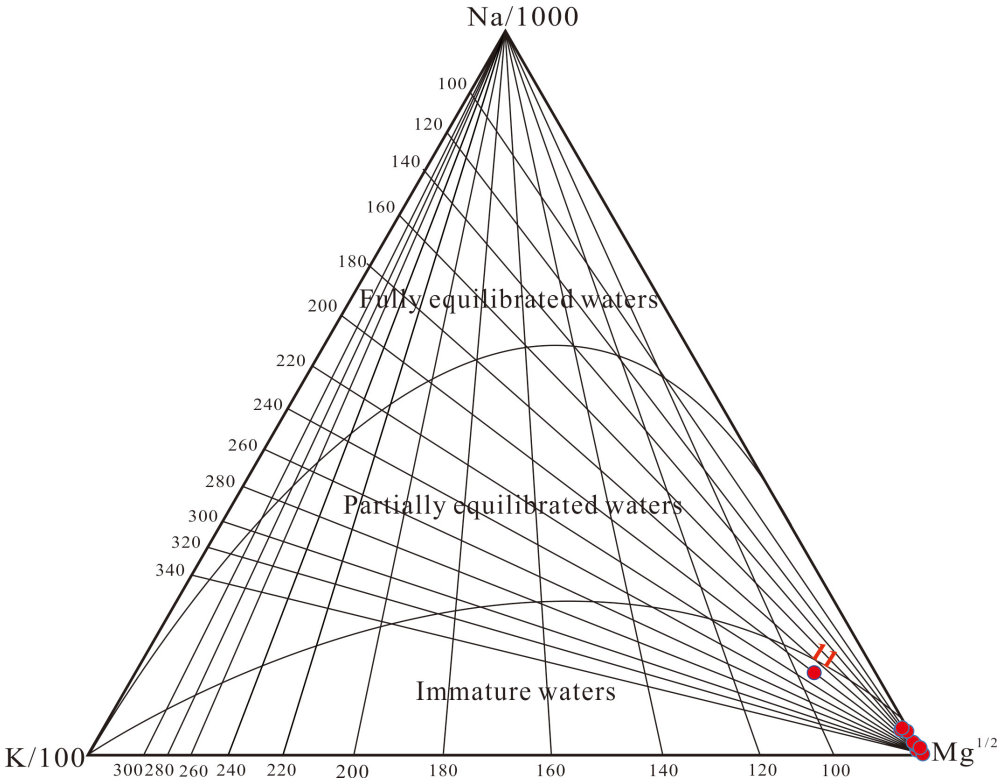

Figure 6. Na–K–Mg triangle diagram.

Preprints.org (www.preprints.org) | NOT PEER-REVIEWED | Posted: 19 March 2024 doi:10.20944/preprints202403.1101.v1

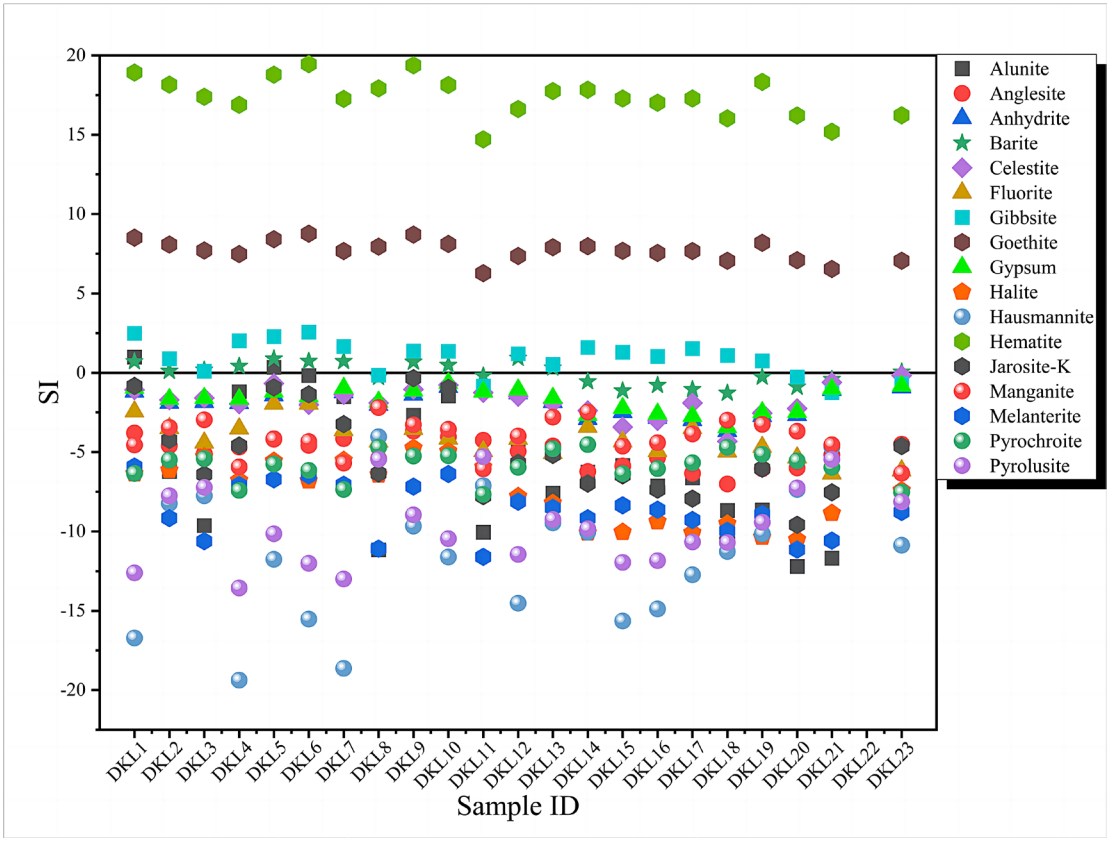

Figure 7. The saturation indexes of varied-temperature springs along the EKF zone at the outflow temperature.

5.4. Trace Elements

The trace element content is generally influenced by lithology, water alkalinity, and human activities. It may also function as a gauge for assessing the extent of water–rock interaction. Different elements have different implications. In our study, we measured 26 types of trace elements, including Ca, Mg, Be, Ag, Cd, Al, Ba, Fe, Co, Cr, Cu, Li, Mo, Mn, Pb, Ni, Sr, Sb, Sn, Th, Ti, Tl, U, V, B, and Zn (see Table 3). It is evident that the content of the same element may vary significantly across different springs. To quantitatively evaluate trace elements, we employed the enrichment factor (*EF*). The *EF* is an important index that quantifies the degree of enrichment of elements. Higher EF values indicate higher degrees of enrichment. The formula for *EF* calculation is as follows:

$$EF_i = (C_i/C_r)_w/(C_i/C_r)_r \quad (2)$$

where C_r represents the content of a selected reference element (Al), C_i represents the content of a specific element in the sample, w represents the concentration of elements in the water sample, and r represents the concentration of elements in the rocks in the study area [57,58].

Figure 8 shows that most trace elements have enrichment factor (*EF*) values less than 1, indicating insufficient water–rock interaction, which aligns with the Na–K–Mg triangle diagram. However, the *EF* values for Fe, Sr, Li, and B are relatively higher compared to other elements. The *EF* values for Fe are all greater than 1, which can be attributed to its mobility in water and the presence of ultramafic rocks in the research region [59]. This discovery aligns with the saturation index. Sr is prone to enrichment in alkaline solutions and its migration is closely linked to Ca. The EF value for Sr in the Tazang segment is greater than 1. Since the Tazang segment is predominantly composed of carbonate lithology containing high levels of Ca^{2+}, and the pH of springs in the area is weakly alkaline, it favors the enrichment of Sr [60]. Li exhibits high chemical reactivity and strong migration ability, making it more prone to enrichment in springs, which indicates deep fluid upwelling [61,62]. The solubility of B in groundwater rises as depth and pressure increase [63]. In the study area, volcanic

Preprints.org (www.preprints.org) | NOT PEER-REVIEWED | Posted: 19 March 2024 doi:10.20944/preprints202403.1101.v1

rocks, sedimentary rocks like sulfates, and sandstones may contain B. When underground water flows through underground volcanic and intrusive rocks, the heating effects (including radioactive isotope heating and residual heat after the formation of volcanic and intrusive rocks) may promote the dissolution of B into groundwater [64]. The B content in groundwater is influenced by factors such as water temperature, flow velocity, and the path through which the water flows within rock layers. Therefore, the B content shows variability among different varied-temperature springs [65–67]. In Figure 8, the highest EF values for Li and B are observed in the Tazang segment, gradually decreasing from the Tazang segment to the Tuosuohu segment. This suggests that the depth of fracture cutting is greater in the southeast compared to the northwest. Additionally, we observed that most other trace elements exhibit higher enrichment in the Tazang, Maqu, and Maqin sections, which can be attributed to deep circulation of the southeast fault and longer water–rock reaction times.

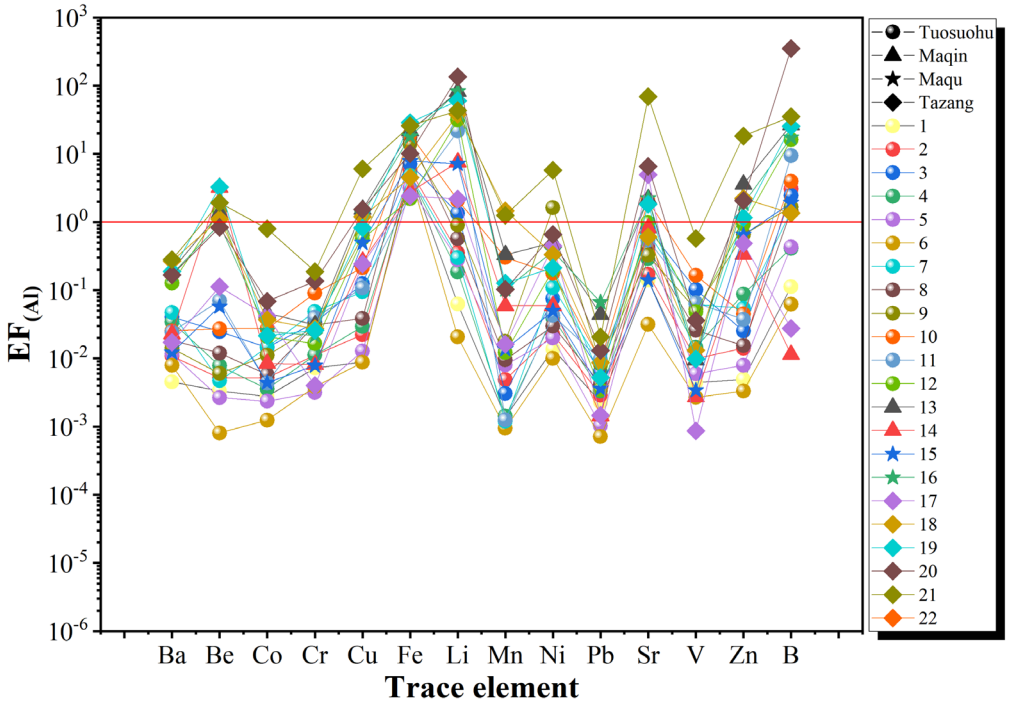

Figure 8. Trace element distribution enrichment coefficient normalized to Al in the spring water.

5.5. Reservoir Temperature and Circulation Depth

Tectonic setting, crustal structure, and properties are the most significant factors influencing the geothermal state. In the Easten Kunlun Fault Zone, Quaternary sedimentary cover in local basins (such as the Xigongzuo Basin and Mohaotang Basin) and the interbedded shales in parts of the Tazang area may have impeded the rapid dissipation of heat to some extent. Additionally, the Himalayan orogeny in the Late Cenozoic, driven by the push of the Indian Plate, generates shear frictional heat within the crust, possibly accompanied by magmatic activities that disturb the geothermal background and create extra heat. Since the Paleozoic, the uplift of intrusive rocks such as A-type granites, with the decay of their radioactive isotopes, also influences crustal heating. Regional faults (like EKLF, KZF, ELSF, and DBF) might connect to deeper heat sources and cause shallow thermal disturbances.

Considering the geological background of the Eastern Kunlun Fault Zone and the temperature and hydrochemical composition of the springs, it is hypothesized that the highlands in the northwest might be the main groundwater recharge area. This region receives atmospheric precipitation and a small amount of meltwater recharge. During infiltration, the decay of radioactive isotopes in granite, the residual heat from magmatic activities since the Permian, active magmatic heat, and frictional heat from tectonic movements might heat the groundwater through thermal conduction. This water

Preprints.org (www.preprints.org) | NOT PEER-REVIEWED | Posted: 19 March 2024 doi:10.20944/preprints202403.1101.v1

is discharged at the surface in the lower terrain of the southeast in the form of springs with varying temperatures and through artificial extraction. Due to the steep slopes in areas like Maqin and Maqu, the relatively low Na/K and Na/Ca ratios might indicate that the cold springs in these areas are fed by shallow recharge from descending springs. In the flatter terrain of the Tazang section, there might still be some ascending springs with deeper circulation and higher temperatures.

The reservoir temperature of varied-temperature water can be predicted based on the chemical composition of water samples. There are two main types of geochemical geothermometers: SiO_2 geothermometers and cation geothermometers. The choice of geothermometer depends on the specific conditions. SiO_2 geothermometers are typically employed in groundwater environments where water–rock interactions are incomplete. To utilize the SiO_2 geothermometers effectively, it is necessary to ensure that the water temperature is ≥25°C, the SiO_2 concentration is ≥11mg/L, and the calculated thermal storage temperature exceeds the spring water temperature [68]. Therefore, considering the inadequate water–rock interaction indicated by the Na–K–Mg triangle diagram (see Figure 6), the reservoir temperature data were evaluated more accurately using the SiO_2 geothermometer equation:

$$T(℃) = \frac{1309}{5.19 - \log(C_{SiO_2})} 273.15 \quad (3)$$

where C_{SiO_2} represents the concentration of SiO_2 in the water [69].

The results of the reservoir temperature calculations are presented in Table 4. In the research region, the classification of most spring waters as cold spring waters is primarily attributed to the mixing of varied-temperature springs with other water bodies during their ascent, which is also a significant factor contributing to incomplete water–rock reactions. [70]. Among all the varied-temperature spring samples, only hot springs Nos. 11, 20, 21, and 23 meet the requirements for using SiO_2 geothermometers, with appropriate SiO_2 concentrations. However, upon observing the data, we found that despite having an SiO_2 concentration lower than 11 mg/l, spring No. 8's concentration is close to 11 mg/l, still indicating its significance in calculating the reservoir temperature in this region. Therefore, to accurately assess the reservoir temperature in this area, we have chosen to consider the calculated results from hot springs Nos. 8, 11, 20, 21, and 23, determined using the SiO_2 geothermometer, as representative of the reservoir temperature in this locality.

Ion geothermometers require the water–rock reactions to reach equilibrium for their applicability. Although the water samples in the research region are considered immature, this does not render the use of ion geothermometers meaningless. The K-Mg geothermometer, which operates under the assumption of rapid equilibrium in water–rock reactions, can be used to estimate the temperature of shallow thermal reservoirs, and still holds valuable indications for non-acidic immature water [71]. Table 4 indicates that the heat storage temperatures calculated using the K-Mg geothermometer are generally low, except for hot spring number 11, which exhibits a significantly higher temperature compared to other springs. This discrepancy is attributed to the precipitation of Mg at high temperatures, leading to an elevated calculated temperature [56]. It is known that within a certain range, deeper circulation corresponds to higher temperatures. Thus, this anomaly suggests that hot spring number 11 has a greater circulation depth and deeper fracture cutting. On the other hand, the Na-K geothermometer relies on the balance between varied-temperature water and alkaline feldspar. When employed to determine the thermal reservoir temperature of immature water, the calculated result often exceeds the actual value. The heat storage temperatures calculated using various geothermometers are summarized in Table 4 [56]. Regarding the heat storage results calculated using the Na-K-Ca and Na-K geothermometers, it can be observed that the heat storage temperatures calculated using the Na-K-Ca geothermometer are higher compared to those calculated using the Na-K geothermometer. This difference is due to the presence of Ca^+ and Mg^+, which can interfere with the accuracy of temperature measurements [72]. From Table 2 of the hydrochemical types, it is evident that this region has a significant concentration of Ca^+ and Mg^+.

Preprints.org (www.preprints.org) | NOT PEER-REVIEWED | Posted: 19 March 2024 doi:10.20944/preprints202403.1101.v1

Table 4. Heat storage temperatures of the varied-temperature fluids calculated using different geothermometers along the mid-eastern part of Eastern Kunlun Fault.

Sample ID	T °C	SiO_2 /mg·L^{-1}	K-Mg	Na-K			Na-K-Ca	Quartz (No Stream Loss)
			a	b	c	d	e	j
EKF1	2.2	4.62	18.2	144.1	89.3	–	199.5	–
EKF2	22.2	0.98	33.5	154.2	100.7	–	225.0	–
EKF3	20	1.79	34.8	127.1	70.4	–	207.3	–
EKF4	6.2	6.09	32.5	180.2	130.9	–	226.1	–
EKF5	15.3	20.60	50.1	165.5	113.6	–	244.2	–
EKF6	4.1	3.88	32.5	165.5	113.7	–	214.1	–
EKF7	7	5.96	43.8	153.8	100.2	–	222.1	–
EKF8	25.9	10.12	40.7	184.1	135.6	–	252.5	–
EKF9	14.5	7.75	39.6	134.1	78.1	–	229.8	–
EKF10	9.3	7.77	43.6	143.5	88.6	–	225.6	–
EKF11	60.4	73.70	94.4	202.6	157.9	–	299.8	121
EKF12	4.5	5.82	21.6	242.2	207.7	–	253.6	–
EKF13	22.2	6.25	33.5	154.2	100.7	–	225.0	–
EKF14	4.5	8.43	27.4	335.8	–	317.9	–	–
EKF15	6.5	8.58	18.9	273.9	249.9	–	–	–
EKF16	6.5	12.46	28.7	306.7	–	289.1	–	–
EKF17	9	6.67	13.1	273.5	249.3	–	–	–
EKF18	4.5	9.24	17.9	259.3	230.2	–	–	–
EKF19	12	8.91	12.3	310.5	–	292.8	–	–
EKF20	28	13.63	22.9	356.4	–	338.4	–	50
EKF21	49	30.92	39.9	270.6	245.4	253.3	296.9	81
EKF22	0	–	18.5	344.0	–	–	310.2	–
EKF23	44.2	22.15	34.6	203.2	158.5	–	248.8	67

Notes: a = K-Mg geothermometer; b = Na-K geothermometer (Giggenbach); c = Na-K geothermometer above 25°C and below 250 °C; d = Na-K geothermometer above 250 °C; e = Na-K-Ca geothermometer; f = Li-Mg geothermometer; j = quartz geothermometer with no stream loss.

It should be noted that the accurate calculation of thermal storage temperatures using ion thermometers relies on the condition of water–rock reaction equilibrium. Under insufficient water–rock reaction conditions in the Eastern Kunlun Fault Zone, it cannot be used to calculate the true thermal storage temperature of the local area. However, it still provides certain indicative significance for the qualitative determination of fault cutting depth, relative temperature differences among different varied-temperature springs, and relative ion concentrations in a specific region. Meanwhile, under the influence of different mineral distribution, water mixing, and suitability conditions for various thermometers, significant variations in thermal storage temperatures calculated by different thermometers are observed, even yielding negative values in cases of low local ion concentrations. The negative values have no practical significance for determining thermal storage temperatures.

The analysis of thermal storage temperatures calculated using SiO_2 geothermometers provides insights into the quantitative calculation of groundwater circulation depth. A more accurate estimation of groundwater circulation depth can be achieved by utilizing the thermal storage temperatures obtained from SiO_2 thermometers for the hot springs numbered 8, 11, 20, 21, and 23 (see Table 5). The calculation formula for groundwater circulation depth is as follows:

$$Z = Z_0 + (T - T_0)/T_{grad} \quad (4)$$

where Z indicates the groundwater circulation depth, Z_0 indicates the isothermal layer depth, T indicates the reservoir temperature (°C), T_0 stands for the temperature of the isothermal layer (°C), and T_{grad} indicates the geothermal gradient (°C/km).

Existing articles on the Eastern Kunlun Fault Zone have conducted limited research on the geothermal parameters within our study area. However, as the Eastern Kunlun Fault Zone serves as the boundary of the Qaidam Basin, its eastern topography and geological lithology bear similarities to our research area and are contiguous with it. Therefore, we have chosen to approximate the geothermal gradient within our study area by utilizing a geothermal gradient of 3.1°C per 100 meters derived from the eastern part of the Qaidam Basin to represent this parameter [74]. In the research

Preprints.org (www.preprints.org) | NOT PEER-REVIEWED | Posted: 19 March 2024 doi:10.20944/preprints202403.1101.v1

region, we assume that the annual average temperature (T_0) in our study area is -3.7°C. The thickness of the isothermal layer (Z_0) refers to the depth at which the range of ground temperature variation is nearly zero. At this depth, the influence of sunlight exposure and seasonal changes is minimal, and the ground temperature remains constant throughout the year. Since Mount Gongga is also located in the eastern part of the Tibetan Plateau, its topographic elevation and temperature are similar to those in the Eastern Kunlun Fault Zone. Therefore, we use the isothermal layer thickness of 30 meters from this region as an approximate value for the isothermal layer thickness in our study area. [20,75].

Table 5. Depths of origin estimated according to reservoir temperatures for geothermal waters in the EKLF zone.

No	Reservoir Temperature/°C	Air Temperature/°C	Circulation Depth/m
8	40	−3.7	1439
11	121	−3.7	4053
20	50	−3.7	1762
21	81	−3.7	2762
23	67	−3.7	2311

5.6. The Proposed Relationship between the Spatial Distribution of Hydrogeochemical Characteristics and Seismicity in the Mid-East Part of EKFZ

Compared to shallow groundwater, springs have larger circulation depths and are less influenced by surface environments and human activities. Hence, they provide better opportunities to obtain earthquake precursor information through the analysis of chemical components in waters. In this study, we divided the middle eastern part of the EKFZ into five sections from west to east: Tuosuohu (EKF 1-EKF 12), Maqin (EKF 13-EKF 14), Xigongzhou, Maqu (EKF 15-EKF 16), and Tazang (EKF 17-EKF 24), based on different fault activity patterns.

To further investigate the relationship between the EKFZ, seismicity, and hydrogeochemistry, the earthquake catalog ($M_L \geq 1$) from May 2021 to May 2023 was selected, which is located near the EKF. The earthquake catalog comes from the China Earthquake Administration (http://10.5.160.18/uniteDayCatalog/index.action). We plot the longitude of water temperature, the focal depth of the earthquake, the earthquake magnitude, the water temperature, the heat storage temperature, the circulation depth, and the slip rate in the same figure (see Figure 9).

Preprints.org (www.preprints.org) | NOT PEER-REVIEWED | Posted: 19 March 2024 doi:10.20944/preprints202403.1101.v1

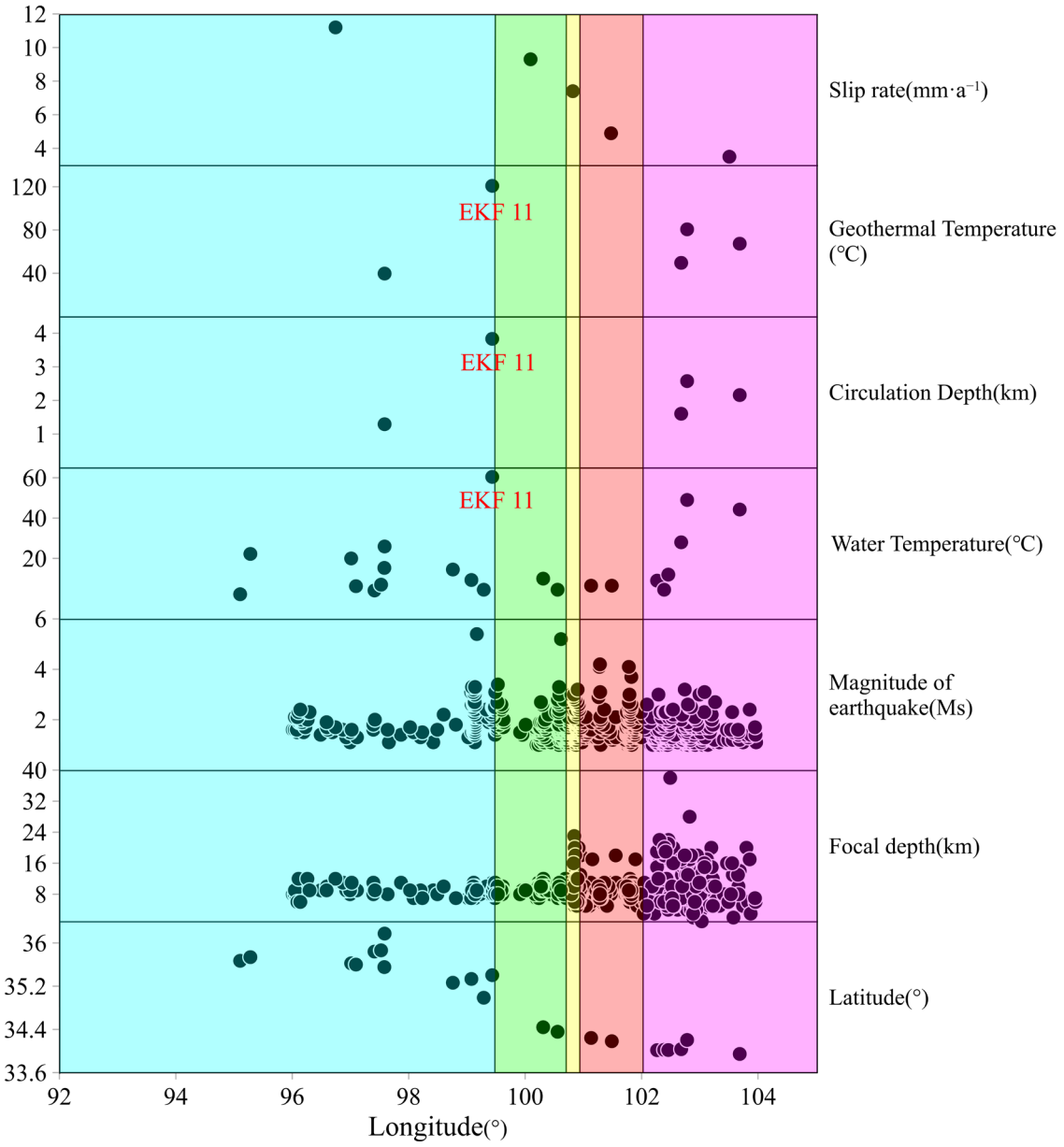

Figure 9. The spatial distribution of slip rate, geothermal temperature, circulation depth, water temperature, magnitude, and focal depth at the mid-eastern part of the EKFZ.

There is a certain correlation between the depth of an earthquake's epicenter and the depth of the water cycle, as well as between the geothermal temperature and the temperature of spring water, with the overall trend being higher in the east and lower in the west. Of course, we have also observed local variations that deviate from this trend. These variations can be attributed to the geological lithology and the mixing effects of different water bodies. As for the special hot spring labeled EKF 11, we will discuss it in detail at the end of this section.

For example, in the Tuosuohu section, the spring temperatures fluctuate, which may be due to the anisotropic nature of the underlying granite and sandstone fractured aquifers. Conversely, the hot springs in the Maqu section exhibit consistently lower temperatures (EKF 15, EKF 16), likely due to a dilution effect from mixing with the Yellow River's surface waters. Considering the springs' proximity to the Yellow River, their reduced temperatures, hydrogen and oxygen isotopes near the local meteoric water line, and strontium isotope ratios close to the river's average, it is reasonable to conclude that these springs are significantly influenced by the Yellow River's waters.

Preprints.org (www.preprints.org) | NOT PEER-REVIEWED | Posted: 19 March 2024 doi:10.20944/preprints202403.1101.v1

In the Maqu–Tazang section, the temperatures of geothermal reservoirs, circulation depths, hot spring temperatures, and seismic source depths overall show a pattern of being higher in the east and lower in the west. This may be related to the widespread distribution of carbonate content in the Maqu–Tazang section. This geological feature facilitates vigorous water–rock interactions and results in greater circulation depths, which in turn lead to elevated geothermal temperatures. Previous studies have suggested that fault activity and deep fluid migration within fault systems may be key controlling factors in regional seismic activity [76]. In deep active fault systems, the increased fluid pore pressure drives fluid flow, reducing the effective normal stress on the fault interface. This weakening of the fracture strength controls seismic activity [77,78]. Moreover, the occurrence of earthquakes enhances water–rock reactions, leading to temperature rises and increased circulation depths. Due to the relatively small slip rate in Tazang section, fluid flow and fluid pressure may be the main mechanisms controlling earthquake generation.

The Xigongzhou segment exhibits relatively high focal depths, likely due to the distribution of tectonic activities. This segment is located in the intersection zone of Xigongzhou, where the slip rate is relatively high. The intensified tectonic activity promotes stronger water–rock reactions, ultimately triggering earthquakes in the deep fracture. The seismic activity in this section may be influenced by the combined effects of hydrothermal and tectonic activities.

In contrast, the Tuosuohu and Maqin areas show fewer occurrences of earthquakes, with shallow hypocenter depths but high magnitudes. The springs in these areas have lower temperatures and shallower circulation depths, resulting in lower thermal storage temperatures. This can be attributed to the substantial presence of granite in this section, which accumulates stress more easily. Additionally, the faults in this section are shallow, leading to weaker water–rock reactions and a smaller weakening effect of fluids on the surrounding rocks. Consequently, stress is released through a few large earthquakes.

Among all the samples, EKF 11 stands out with the highest hot spring temperature, calculated to be 120.83°C using a silica geothermometer, suggesting that it may have the deepest circulation depth and a significant occurrence of small earthquakes in its vicinity. This can be attributed to the location of EKF 11 at the intersection of two faults (ELSF and KZF), as illustrated in Figure 10. The deep fractures in this area, coupled with the strong reaction between the high-temperature spring water and the surrounding rock, play a significant role in weakening the rock structure, making it more prone to small earthquakes. Additionally, it is important to note that this calculated value only serves as an indication of a potential deep thermal source and has not been verified by direct drilling data.

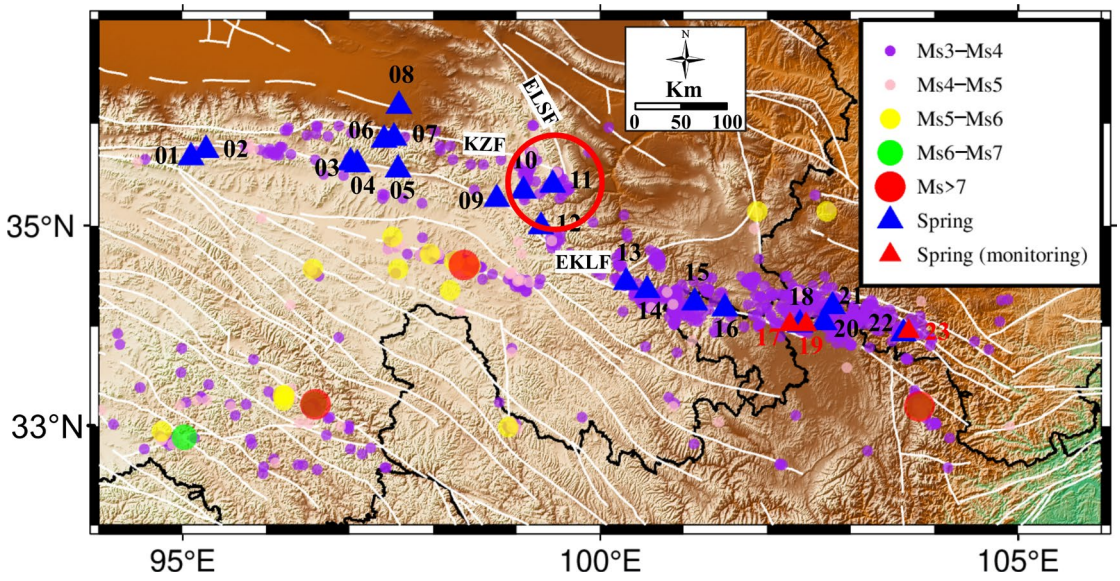

Preprints.org (www.preprints.org) | NOT PEER-REVIEWED | Posted: 19 March 2024 doi:10.20944/preprints202403.1101.v1

Figure 10. Spatial distribution of varied-temperature springs and earthquakes in the EKLF. The red dotted circle box selects earthquakes within 50km of EKF 11 hot spring (the solid circle represents earthquakes with $M_S \geq 3.0$ since 2012.).

5.7. Temporal Variation Characteristics of Springs and Response to the Earthquake

The occurrence of earthquakes has a profound impact on the stress–strain condition of fault zones, consequently affecting the characteristics of aquifers. Typically, an enlarged water–rock reaction surface, the mixing of diverse water bodies, and the release of deep geothermal fluids are associated with an increase in the porosity of fault zones [80]. The influence of earthquakes on the stress–strain state can be categorized into two types: static action and dynamic action. Static action primarily influences fault activity, while dynamic action is mainly manifested through the impact of seismic waves on aquifers. This indicates that an earthquake's process of development involves the accumulation of stress followed by a sudden stress release, leading to alterations in ion concentration prior to and after the event [81,82].

It is acknowledged that intra-annual seasonality and regional precipitation patterns can impact ion concentration variations. While our study did not measure seasonal changes, precipitation, spring water discharge, and temperature data during the sampling period, we have supplemented our analysis with data from three continuous monitoring stations from June 30, 2021, to June 17, 2023. During this extended period, we observed that in times of minor or no seismic activity, ion concentrations fluctuated only around the mean value. This pattern suggests that while there may be some degree of influence from seasonal variations and precipitation on ion concentrations, these factors have a minimal impact on the anomalies associated with seismic activity, to the extent that their effects can be considered negligible for the purposes of our study. Hence, our findings support the premise that monitoring ion concentration changes could potentially aid in earthquake prediction.

Na^+, Cl^-, SO_4^{2-}, Ca^{2+}, HCO_3^-, K^+, and F^+ have been identified as sensitive indicators of earthquakes [12,20,83–85]. However, Ca^{2+} and HCO_3^- are prone to precipitation, K^+ can be easily adsorbed by soil, and the F^- concentration is below the detection limit. Thus, only Na^+, Cl^-, and SO_4^{2-} are used to monitor earthquakes in this study.

Continuous monitoring of major anions and cations was conducted at Maqu (EKF 17), Maixi (EKF 19), and Jiulongxia (EKF 23) stations every three days. The monitoring period for Maqu Station (EKF 17) was 30 June 2021–21 October 2023. The monitoring period for Maixi Station (EKF 19) was 21 June 2021–30 September 2023. The monitoring period for Jiulongxia Station (EKF 23) was 16 August 2021–17 June 2023. To assess outliers of ion concentrations, the standard deviation (σ) was used. The mean (μ) ± double standard deviation (2σ) was employed as the upper and lower bounds for positive and negative exceptions, respectively. The monitoring results are presented in Figure 11 and Table 6. It is worth noting that earthquakes with an $M_S \leq 4$ have no significant impact on ion concentrations [86]. For earthquakes above magnitude 4 within a 400 km radius of the continuous monitoring stations, please refer to Supplementary Table S1 (https://data.earthquake.cn/datashare/report.shtml?PAGEID=earthquake_zhengshi).

The analysis of Figure 11 reveals that seismic activities near most of the continuous monitoring stations do not exhibit significant changes in water chemical components, indicating a limited response to earthquakes. However, regional earthquakes with a magnitude of MS≥4 within a 400 km radius of the monitoring stations may lead to changes in groundwater composition within the area. This paper analyzes three regional earthquakes that occurred during the monitoring period in the Eastern Kunlun Fault region: the Gande M_S 4.7 earthquake on December 6, 2021, the Maerkang M_S 6.0 earthquake on June 10, 2022, and the Maduo M_S 5.0 earthquake on December 22, 2022. These earthquakes are characterized by their shallow hypocenters, significant magnitudes, and proximity to continuous monitoring stations.

Among the three regional earthquakes, despite the Gande earthquake having the smallest magnitude, Na^+, Cl^-, and SO_4^{2-} showed sensitivity to earthquakes at all three continuous monitoring stations. Remarkably, 46 days prior to the Gande earthquake, there was a notable rise in the concentration of Cl^- and Na^+ in the Maqu continuous monitoring data. This can be attributed to the

Preprints.org (www.preprints.org) | NOT PEER-REVIEWED | Posted: 19 March 2024 doi:10.20944/preprints202403.1101.v1

fact that the continuous monitoring station and the Gande earthquake were both situated in the EKFZ. Consequently, there was an interaction between different segments of the EKFZ, and the Gande earthquake induced stress–strain loading in adjacent sections [15]. Furthermore, by examining the variation in Cl^- concentration before the Gande earthquake, it is evident that within the same fault system, the anomalies appeared earlier at monitoring stations closer to the epicenter. In the continuous monitoring results of Maqu station, the concentrations of Na^+, Cl^-, and SO_4^{2-} exhibit a similar trend, indicating the influence of the target earthquake. This phenomenon can be attributed to preseismic dilation [11,84].

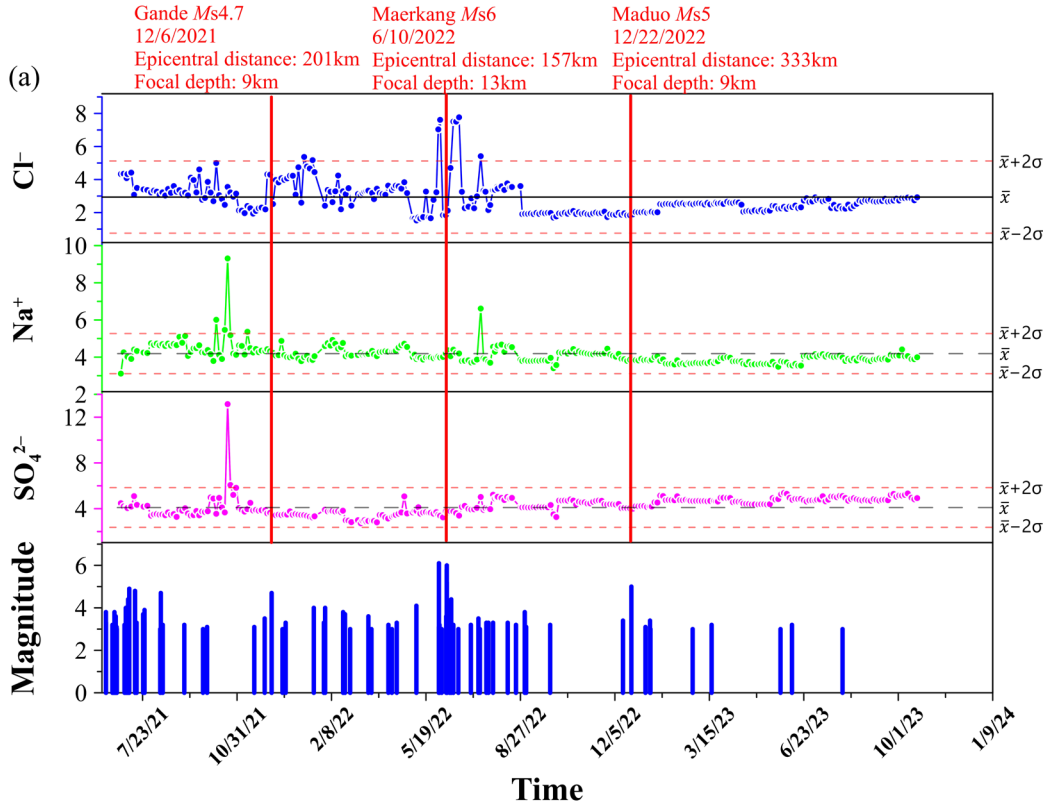

Preprints.org (www.preprints.org) | NOT PEER-REVIEWED | Posted: 19 March 2024 doi:10.20944/preprints202403.1101.v1

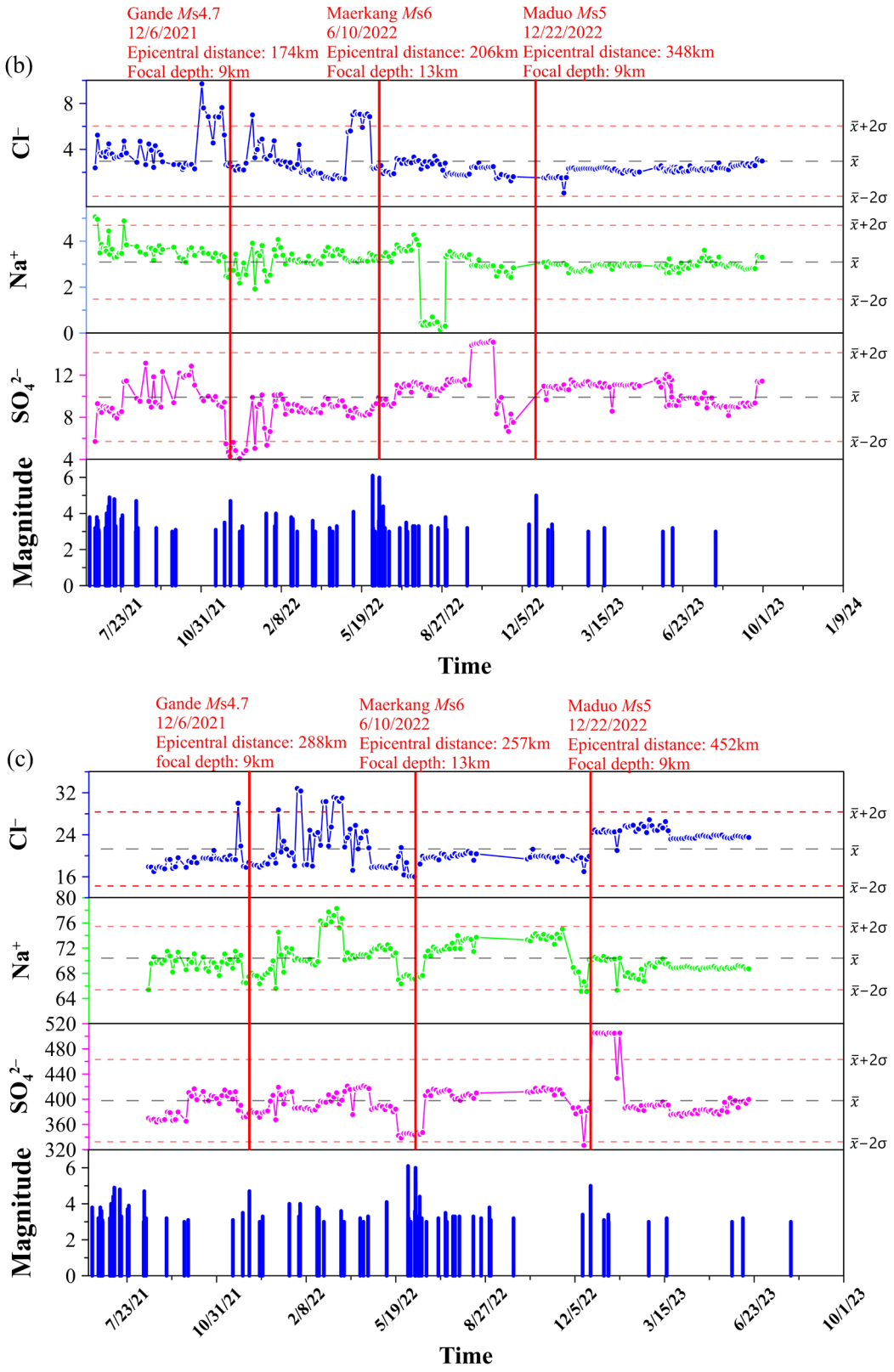

Figure 11. Temporal variations in the concentration of Cl^-, Na^+ and SO_4^{2-} related to earthquakes. (**a**) The Maqu spring (EKF17); (**b**) the Maixi spring (EKF 19); and (**c**) the Jiulongxia spring (EKF23).

Preprints.org (www.preprints.org) | NOT PEER-REVIEWED | Posted: 19 March 2024 doi:10.20944/preprints202403.1101.v1

Table 6. The occurrence time of precursory and post-seismic anomalies in the continuous monitoring sites before three earthquakes.

Monitoring Sites	Changes		2021 Gande *Ms* 4.7		2022 Maerkang *Ms* 6.0		2022 Maduo *Ms* 5.0	
			Precursory Anomaly	Post-Seismic Anomalies	Precursory Anomaly	Post-Seismic Anomalies	Precursory Anomaly	Post-Seismic Anomalies
EKF 17	Cl^-	multiple	2.6 ↑	2.4 ↑	5.1 ↑	5 ↑	—	—
	Na^+		2.5 ↑	—	—	—	1.7 ↑	—
	SO_4^{2-}		4 ↑	—	1.8 ↑	—	—	—
	Epicenter distance	(km)	201		157		333	
EKF 19	Cl^-	multiple	4.2 ↑	3 ↑	4.8 ↑	—	—	—
	Na^+		2.1 ↓	—	—	—	6.5 ↓	—
	SO_4^{2-}		2.8 ↓	2.4 ↑	—	—	2.3 ↓	—
	Epicenter distance	(km)	174		206		348	
EKF 23	Cl^-	multiple	1.6 ↑	—	2 ↑	—	—	—
	Na^+		1.1 ↑	—	1.2 ↓	—	1.2 ↓	—
	SO_4^{2-}		—	—	1.2 ↓	—	1.3 ↓	1.3 ↑
	Epicenter distance	(km)	288		257		452	

Notes: "↑" represents the amplification of ion concentration. "—" represents not over anomaly threshold.

Before the occurrence of the Maerkang earthquake, there were notable increases in the Cl^- concentration at the three continuous monitoring stations. The concentration of Cl^- rose by 2.9 times. It is important to note that Cl^- is an indicator of deep fluid upwelling and is less influenced by the mixing of shallow cold water. This observation aligns with previous studies, such as the 1995 Galicia earthquake in Spain, where the concentration of Cl^- in well water nearly doubled [13]. Similarly, during the Koyna *Ms* 5.1 earthquake on 5 March 2005, the well water around the Koyna and Warna reservoirs in India exhibited a doubling in Cl^- concentration, a tripling in SO_4^{2-} concentration, and a sevenfold increase in F^- concentration, while $\delta^{18}O$ values showed a decreasing trend [87]. Additionally, Zhou et al. reported a significant upward trend in SO_4^{2-} and Cl^- concentrations before the Yangbi *Ms* 6.4 earthquake [3]. These observations suggest that at fault depths, the pressure promotes the movement of fluids from the deep rock medium along the fault to the aquifer. This process leads to water mixing and hydrogeochemical changes, disrupting the original system equilibrium [88].

The Maduo earthquake (*Ms* = 5) is the closest to the Maqu continuous monitoring station; however, the fluctuation range of Na^+, Cl^-, and SO_4^{2-} at Maqu is relatively small. This can be attributed to the fact that the Maqu monitoring station is outside the tectonic system where the earthquake occurs. At the Maixi continuous monitoring station, abnormal values of SO_4^{2-} and Na^+ were the first to appear, whereas at the Jiulongxia continuous monitoring station, abnormal values were observed only after the earthquake. This difference may be related to the distance from the epicenter. The distance between the earthquake source and Jiulongxia is quite great, and therefore the stress accumulation was not effectively transmitted to the Jiulongxia continuous monitoring station prior to the earthquake. After the earthquake occurred, the stress was effectively transferred to the monitoring station. Meanwhile, we discovered that the changes in water chemical composition

Preprints.org (www.preprints.org) | NOT PEER-REVIEWED | Posted: 19 March 2024 doi:10.20944/preprints202403.1101.v1

caused by the Maduo earthquake were relatively small compared to those caused by other earthquakes, mainly because this earthquake was an aftershock. The response of hydrochemical components to earthquakes is influenced by various factors, including the distance from the epicenter, the earthquake's magnitude, the tectonic location, and the earthquake type. Furthermore, the stress generated by an earthquake exhibits characteristics of anisotropy during transmission.

5.8. The Hydrogeochemical Circulation Model of varied-temperature Spring Waters in the Mid-Eastern Part of the EKFZ

Understanding the source and movement of groundwater in seismically active regions is crucial for investing hydrogeochemical indicators in the central and eastern EKFZ [87]. The EKFZ exhibits well-developed fractures, which facilitate the infiltration of different water bodies and the upwelling of deep fluids. In this section, we introduce a conceptual model of hydrogeochemistry in the EKFZ, integrating hydrogeochemical features, spring circulation depth, recharge elevation, and reservoir temperature (see Figure 12).

The analysis of hydrogen and oxygen isotopes indicates a significant evaporative effect in the EKFZ, with atmospheric precipitation being the primary source of replenishment for varied-temperature springs near the fault zone. The replenishment zone is estimated to be at an elevation of 1.0–2.8 km. Some springs, such as EKF 1 and EKF 7, may have mixed with snowmelt water from nearby snow mountains, while EKF 23 may be replenished by deep water within the fault zone. Springs like EKF 3, EKF 5, EKF 8, EKF 9, and EKF 11 exhibit deeper groundwater circulation and longer water–rock reaction times. Atmospheric precipitation converges at the surface and infiltrates along the fracture zones to recharge groundwater, with circulation depths ranging from 1.29 to 3.83 km. The southeastern section shows higher enrichment of B and Li, with a greater circulation depth of varied-temperature spring water compared to the northwestern section. The EKF 11 hot spring, situated at the intersection of two fault zones, exhibits the deepest groundwater circulation, reaching a depth of 3.83 km. During this deep underground circulation, the groundwater undergoes constant heating due to the water–rock interaction. The temperature range of heat storage varies from 39.64 °C to 120.83 °C, with the main heat sources being magmatic heat, granite radiation heat, and sliding friction heat within the fault zone [90]. In terms of heat sources within the study area, the radioactive decay within the exposed granite may release heat over time, contributing to the overall geothermal budget of the region. This decay process impacts the thermal state of groundwater as it percolates through granite-rich strata, thereby affecting the temperature of the springs in these terrains [33,34]. Additionally, the ongoing uplift of the Tibetan Plateau and the movement of the Indian Plate ensure that the Eastern Kunlun Fault Zone is still sliding at a certain rate. The frictional heat generated from this shear movement serves as another significant geothermal contributor, which can directly elevate the temperatures of groundwater circulating near the fault zones, leading to higher spring temperatures in these areas. The heat produced by magmatic activities is an essential source for the deep thermal environment. The residual heat from magmatic activities since the Paleozoic era, along with potential ongoing magmatic activities, transfers from the magma to the surrounding rock and then to the groundwater by conduction, affecting the higher temperature ranges of the springs [35,36]. It is important to note that, due to the scarcity of hydrogeological data in this region and the absence of measurements such as flow rate, velocity, temperature variations, and drilling data in our study, we can only roughly estimate the potential heat sources for the overall spring waters in the Eastern Kunlun Fault Zone. This limitation prevents a detailed analysis of the primary heat source for each individual spring. Based on the generally low air temperatures of the springs and the predominance of immature waters in the EKFZ, we speculate that the influence of current magmatic activity in this area is minimal. Alternatively, it might be because the thicker crust beneath the EKFZ suggests that magmatic activities may occur at greater depths, thereby exerting a lesser impact on the springs. Under specific temperature and pressure conditions, water reacts with surrounding rocks such as carbonate, gypsum, etc.

There are 11 distinct types of water chemistry in the region, primarily determined by the composition of the surrounding rocks. These include Na-Mg-HCO_3-Cl, Mg-SO_4-HCO_3, Na-Cl, Na-

Preprints.org (www.preprints.org) | NOT PEER-REVIEWED | Posted: 19 March 2024 doi:10.20944/preprints202403.1101.v1

HCO_3, Na-Ca-Cl-HCO_3, Ca-Na-HCO_3, Na-Cl-SO_4, Na-Mg-Cl, Na-SO_4, Ca-HCO_3, and Ca-Mg-HCO_3. In the Tuosuohu area, the main ions present are Na^{2+}, Ca^{2+}, HCO_3^-, and Cl^-, with a significant distribution of sandstones. In the Maqin, Maqu, and Tazang regions, the main ions are Mg^{2+}, Ca^{2+}, and HCO_3^-, with a prominent presence of granites and carbonates. Water samples from the area are considered immature. In regions with greater circulation depth, faults are weakened due to hydrostatic pressure and water–rock reactions, leading to the frequent occurrence of smaller earthquakes in Tuosuohu and Tazang. The Maqin–Maqu section near Tazang serves as a transitional area with geothermal anomalies, indicating the possibility of a significant earthquake in this region.

The hot water in the fault water channel circulates upwards due to the pressure difference. During this ascent, the EKF 3, EKF 8, EKF 15, and EKF 21 springs mix with surface water to varying degrees. As the hot water rises, significant quantities of hematite minerals and goethite minerals precipitate. The northwestern mountainous area is notably higher than the southeastern section. The spring water in the Maqin, Maqu, and Tazang regions may originate from a descent spring fed by an aquifer located in front of a mountain.

Ultimately, the groundwater surfaces as varied-temperature water. Before and after the Maduo *M*s 5.0 earthquake, Maerkang *M*s 6.0 earthquake, and Gande *M*s 4.7 earthquake, there were anomalies in the water chemistry observed at three continuous monitoring stations in Maqin, Maixi, and Jiulongxia. Underground fluid serves as an effective indicator of earthquake preparation and occurrence, contributing to the establishment of a conceptual model of hydrogeochemistry. This model plays a vital role in comprehending the causes of earthquakes and aiding in short-term earthquake prediction.

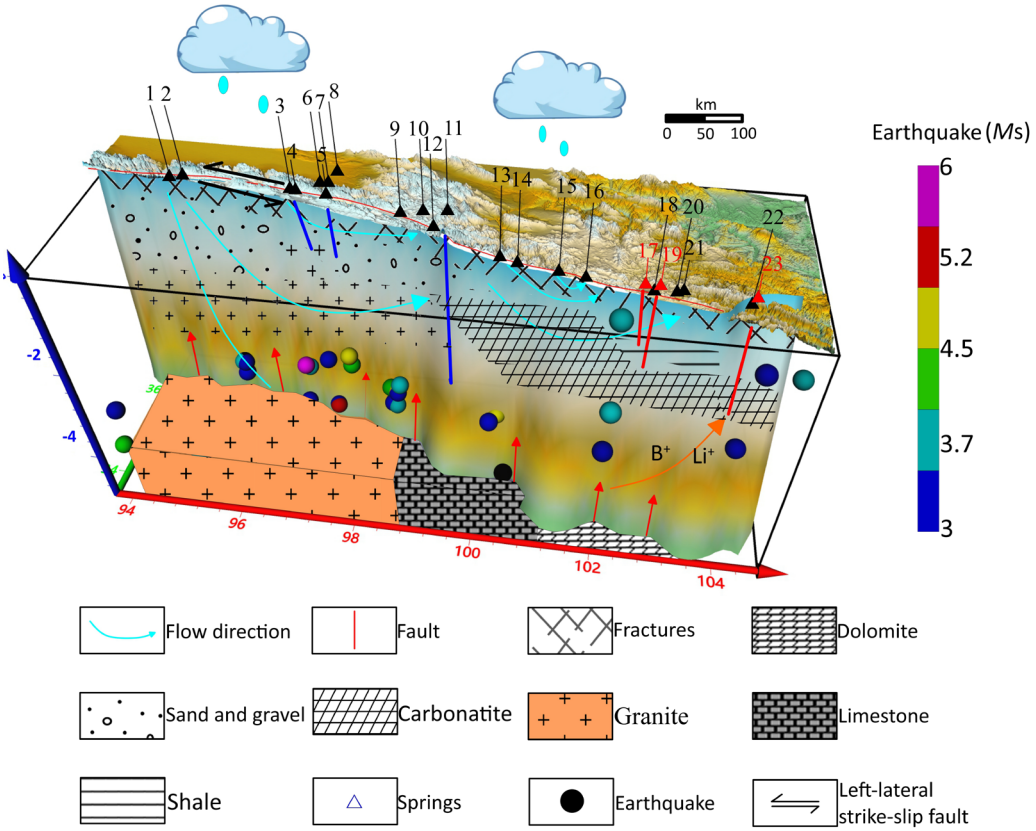

Figure 12. The conceptual hydrothermal model of the hydrogeochemical cycling process in high-temperature geothermal systems along the EKF. The numbers "1-23" represent the sampling numbers of the varied-temperature springs. Circles of different colors represent earthquake magnitudes of varying sizes.

Preprints.org (www.preprints.org) | NOT PEER-REVIEWED | Posted: 19 March 2024 doi:10.20944/preprints202403.1101.v1

6. Conclusions

This research aimed to fill the knowledge gap regarding the hydrogeochemical characteristics of varied-temperature springs along the east-central section of the Eastern Kunlun Fault Zone (EKFZ), with a particular focus on understanding the implications of these characteristics for earthquake prediction and monitoring. The study's primary objective was to examine the interplay between hydrogeochemistry and seismic activity within this seismically active region.

The methodology involved sampling 23 varied-temperature springs across the EKFZ from May to July 2021, employing both census and detailed survey techniques. This approach enabled the collection of 609 water samples, with subsequent laboratory analysis focusing on a range of parameters, including major and trace element concentrations, isotope ratios, and mineral saturation indexes. The study's key setting was its focus on an area known for its seismic activity and complex geological structure, making it an ideal location for examining the connections between groundwater geochemistry and earthquakes.

The research findings highlight several critical points:

1. The springs' water chemistry indicates a primary origin from atmospheric precipitation, with significant evaporative effects observed.

2. Isotopic analysis revealed a decreasing concentration of hydrogen and oxygen isotopes from west to east, suggesting variations in evaporation and water–rock interactions across the fault zone.

3. The study identified 11 distinct water chemistry types, reflecting the diverse lithology of the region.

4. The reservoir temperatures of the springs, ranging from 39.64°C to 120.83°C, along with their varied circulation depths (1.29 to 3.83 km), underscore the complex interaction between geothermal activity and groundwater movement in the EKFZ.

5. Notably, the hydrogeochemical changes observed before and after seismic events such as the Maerkang and Maduo earthquakes suggest a potential for using groundwater chemistry as an indicator for earthquake prediction.

The study's limitations include its relatively short duration and the focus on a specific segment of the EKFZ. These factors may restrict the generalizability of the findings and underscore the need for longer term and broader geographic studies to fully understand the hydrogeochemical dynamics of the fault zone.

Despite these limitations, the research significantly contributes to our understanding of the interplay between hydrogeochemistry and seismic activity in the EKFZ. It offers valuable insights for earthquake monitoring and prediction in seismically active regions, enhancing our ability to assess seismic hazards and mitigate their impacts. The study's findings also suggest potential engineering applications, such as the development of early warning systems based on hydrogeochemical indicators, which could significantly enhance public safety and infrastructure resilience in earthquake-prone areas.

In conclusion, this research not only advances our knowledge of the hydrogeochemical characteristics of varied-temperature springs in the EKFZ but also underscores the importance of integrating hydrogeochemical analysis into seismic hazard assessment and earthquake prediction strategies. Future research should aim to expand upon these findings, exploring the broader implications of hydrogeochemical changes for understanding seismic processes and enhancing earthquake preparedness in similar tectonic settings.

Supplementary Materials: The following supporting information can be downloaded at the website of this paper posted on Preprints.org.

Author Contributions: Conceptualization, C.L., X.Z. (Xiaocheng Zhou), and J.J.; methodology, C.L. and X.Z. (Xiaocheng Zhou); software, C.L. and X.Z. (Xiaoyi Zhu); validation, C.L., X.Z. (Xiaocheng Zhou), and J.J.; formal analysis J.L (Jingchao Li)., J.L. (Jing Li), and X.Z. (Xiaocheng Zhou); investigation, J.W., G.X., J.L.(Jiang Li), and S.C.; data curation, C.L., G.X., and S.C.; writing—original draft preparation, C.L., X.Z. (Xiaocheng Zhou), and J.J.; writing—review and editing, C.L. and X.Z. (Xiaocheng Zhou); visualization, C.L.; supervision, X.Z. (Xiaocheng Zhou); project administration, C.L., X.Z. (Xiaocheng Zhou) and J.J.; All authors have read and agreed to the published version of the manuscript.

Preprints.org (www.preprints.org) | NOT PEER-REVIEWED | Posted: 19 March 2024 doi:10.20944/preprints202403.1101.v1

Funding: The work was funded by the National Key Research and Development Project (2023YFC3012005, 2022YFC2204301, 2018YFE0109700, 2019YFC1509203), the Central Public Interest Scientific Institution Basal Research Fund (CEAIEF2022030200, CEAIEF2022030205, CEAIEF20220507, CEAIEF20230602, CEAIEF20230503), the National Natural Science Foundation of China (41673106, 42073063, 4193000170, U2039207), the Open Foundation of the United Laboratory of High Pressure Physics and Earthquake Science (2022HPPES05), IGCP Project 724 and Science and Technology Innovation Program for Postgraduate students in IDP subsidized by Fundamental Research Funds for the Central Universities (CXZZSS2023186).

Data Availability Statement: The raw data supporting the conclusions of this article will be made available by the authors, without undue reservation.

Conflicts of Interest: The authors declare no conflicts of interest.

References

1. Chiodini, G.; Cardellini, C.; Di Luccio, F.; Selva, J.; Frondini, F.; Caliro, S.; Rosiello, A.; Beddini, G.; Ventura, G. Correlation between tectonic CO2 Earth degassing and seismicity is revealed by a 10-year record in the Apennines, Italy. *Sci. Adv.* **2020**, *6*, eabc2938. https://doi.org/10.1126/sciadv.abc2938.
2. Tanikawa, W.; Sakaguchi, M.; Tadai, O.; Hirose, T. Influence of fault slip rate on shear-induced permeability. *J. Geophys. Res.-Solid Earth* **2010**, *115*, 18. https://doi.org/10.1029/2009jb007013.
3. Zhou, H.L.; Zhou, X.C.; Su, H.J.; Li, Y.; Liu, F.L.; Ouyang, S.P.; Yan, Y.C.; Bai, R.L. Hydrochemical Characteristics of Earthquake-Related Thermal Springs along the Weixi-Qiaohou Fault, Southeast Tibet Plateau. *Water* **2022**, *14*, 132. https://doi.org/10.3390/w14010132.
4. Scott, B.E.; Newell, D.L.; Jessup, M.J.; Grambling, T.A.; Shaw, C.A. Structural Controls on Crustal Fluid Circulation and Hot Spring Geochemistry above a Flat-Slab Subduction Zone, Peru. *Geochem. Geophys. Geosyst.* **2020**, *21*, e2020GC008919. https://doi.org/10.1029/2020gc008919.
5. Tian, J.; Pang, Z.H.; Liao, D.W.; Zhou, X.C. Fluid geochemistry and its implications on the role of deep faults in the genesis of high temperature systems in the eastern edge of the Qinghai Tibet Plateau. *Appl. Geochem.* **2021**, *131*, 105036. https://doi.org/10.1016/j.apgeochem.2021.105036.
6. Lowell, R.P. A fault-driven circulation model for the Lost City Hydrothermal Field. *Geophys. Res. Lett.* **2017**, *44*, 2703–2709. https://doi.org/10.1002/2016gl072326.
7. Liu, B.; Yan, G.; Ma, Y.; Scheuermann, A. Measurement of In-Situ Flow Rate in Borehole by Heat Pulse Flowmeter: Field-Case Study and Reflection. *Geosciences* **2023**, *13*, doi:10.3390/geosciences13050146.
8. Bo, Y.; Liu, C.L.; Zhao, Y.J.; Wang, L.C. Chemical and isotopic characteristics and origin of spring waters in the Lanping-Simao Basin, Yunnan, Southwestern China. *Chem. Der Erde-Geochem.* **2015**, *75*, 287–300. https://doi.org/10.1016/j.chemer.2015.04.002.
9. Zhou, X.C.; Yan, Y.C.; Fang, W.Y.; Wang, W.L.; Shi, H.Y.; Li, P.F. Short-Term Seismic Precursor Anomalies of Hydrogen Concentration in Luojishan Hot Spring Bubbling Gas, Eastern Tibetan Plateau. *Front. Earth Sci.* **2021**, *8*, 586279. https://doi.org/10.3389/feart.2020.586279.
10. Zhou, X.C.; Liu, L.; Chen, Z.; Cui, Y.J.; Du, J.G. Gas geochemistry of the hot spring in the Litang fault zone, Southeast Tibetan Plateau. *Appl. Geochem.* **2017**, *79*, 17–26. https://doi.org/10.1016/j.apgeochem.2017.01.022.
11. Skelton, A.; Andren, M.; Kristmannsdottir, H.; Stockmann, G.; Morth, C.M.; Sveinbjornsdottir, A.; Jonsson, S.; Sturkell, E.; Gudorunardottir, H.R.; Hjartarson, H.; et al. Changes in groundwater chemistry before two consecutive earthquakes in Iceland. *Nat. Geosci.* **2014**, *7*, 752–756. https://doi.org/10.1038/ngeo2250.
12. Gori, F.; Barberio, M.D. Hydrogeochemical changes before and during the 2019 Benevento seismic swarm in central-southern Italy. *J. Hydrol.* **2022**, *604*, 127250. https://doi.org/10.1016/j.jhydrol.2021.127250.
13. Perez, N.M.; Hernandez, P.A.; Igarashi, G.; Trujillo, I.; Nakai, S.; Sumino, H.; Wakita, H. Searching and detecting earthquake geochemical precursors in CO2-rich groundwaters from Galicia, Spain. *Geochem. J.* **2008**, *42*, 75–83. https://doi.org/10.2343/geochemj.42.75.
14. Barbieri, M.; Franchini, S.; Barberio, M.D.; Billi, A.; Boschetti, T.; Giansante, L.; Gori, F.; Jonsson, S.; Petitta, M.; Skelton, A.; et al. Changes in groundwater trace element concentrations before seismic and volcanic activities in Iceland during 2010–2018. *Sci. Total Environ.* **2021**, *793*, 148635. https://doi.org/10.1016/j.scitotenv.2021.148635.
15. Li, C.X.; Xu, X.W.; Wen, X.Z.; Zheng, R.Z.; Chen, G.H.; Yang, H.; An, Y.F.; Gao, X. Rupture segmentation and slip partitioning of the mid-eastern part of the Kunlun Fault, north Tibetan Plateau. *Sci. China-Earth Sci.* **2011**, *54*, 1730–1745. https://doi.org/10.1007/s11430-011-4239-5.
16. Zhu, L.; Ji, L.; Liu, C. Interseismic slip rate and locking along the Maqin–Maqu Segment of the East Kunlun Fault, Northern Tibetan Plateau, based on Sentinel-1 images. *J. Asian Earth Sci.* **2021**, *211*, 104703. https://doi.org/10.1016/j.jseaes.2021.104703.
17. Zhang, J.L.; Ren, J.W.; Chen, C.Y.; Fu, J.D.; Yang, P.X.; Xiong, R.W.; Hu, C.Z. The Late Pleistocene activity of the eastern part of east Kunlun fault zone and its tectonic significance. *Sci. China-Earth Sci.* **2014**, *57*, 439–453. https://doi.org/10.1007/s11430-013-4759-2.

Preprints.org (www.preprints.org) | NOT PEER-REVIEWED | Posted: 19 March 2024 doi:10.20944/preprints202403.1101.v1

18. Ma, Y.S.; ShI, W.; Zhang, Y.Q.; Yang, N.; Zhang, C.S.; Zhang, H.P. Characteristics of the activity of the Maqu segment of the East Kunlun active fault belt and its eastward extension. *Geol. Bull. China* **2005**, *24*, 30–35. (In Chinese)
19. Luo, Z.B.; Zhou, X.C.; He, M.; Liang, J.L.; Li, J.C.; Dong, J.Y.; Tian, J.; Yan, Y.C.; Li, Y.; Liu, F.L.; et al. Earthquakes evoked by lower crustal flow: Evidence from hot spring geochemistry in Lijiang-Xiaojinhe fault. *J. Hydrol.* **2023**, *619*, 129334. https://doi.org/10.1016/j.jhydrol.2023.129334.
20. Yan, Y.C.; Zhou, X.C.; Liao, L.X.; Tian, J.; Li, Y.; Shi, Z.M.; Liu, F.L.; Ouyang, S.P. Hydrogeochemical Characteristic of Geothermal Water and Precursory Anomalies along the Xianshuihe Fault Zone, Southwestern China. *Water* **2022**, *14*, 550. https://doi.org/10.3390/w14040550.
21. Seismologic Bureau of Qinghai Province, the Institute of Crustal Dynamics of China Earthquake. *Eastern Kunlun Active Fault Zone*; Seismological Press: Beijing, China, 1999. (In Chinese)
22. Guo, J.; Lin, A.; Sun, G.; Zheng, J. Surface Ruptures Associated with the 1937 M 7.5 Tuosuo Lake and the 1963 M 7.0 Alake Lake Earthquakes and the Paleoseismicity along the Tuosuo Lake Segment of the Kunlun Fault, Northern Tibet. *Bull. Seismol. Soc. Am.* **2007**, *97*, 474–496. https://doi.org/10.1785/0120050103.
23. Jerome, V.D.W.; Paul, T.; Frederick, J.R.; Anne-Sophie, M.; Bertrand, M.; Yves, G.; Robert, C.F.; Marc, W.C.; Zhao, G.G.; Xu, Z. Uniform psotglacial slip-rate along the central 600 km of the Kunlun Fault (Tibet), from 26Al, 10Be, and 14C dating of riser offsets, and climatic origin of the regional morphology. *Geophys. J. Int.* **2002**, *148*, 356–388.
24. Li, C.; He, Q.; Zhao, G. Holocene slip rate along the eastern segment of the Kunlun fault. *Seismol. Geol.* **2004**, *26*, 676–687.
25. Liu, G.X. Eastern Kunlun Active Fault Zone and Its Seismic Activity. *Earth Res. China* **1996**, *12*, 119–126.
26. Li, C.-f.; He, Q.-l.; Zhao, G.-g. Paleo-earthquake studies on the eastern section of the Kunlun fault. *Acta Seismol. Sin.* **2005**, *18*, 64–71. https://doi.org/10.1007/s11589-005-0007-y.
27. Li, C.X. The Long-Trem Faulting Behavior of the Eastern Segment (Maqin-Maqu) of the East Kunlun Faults Since Ther Late Quaternary. Ph.D. Thesis, Institute of Geology of China Earthquake Administration, Beijing, China, 2009.
28. Lin, A.M.; Guo, J.M. Nonuniform Slip Rate and Millennial Recurrence Interval of Large Earthquakes along the Eastern Segment of the Kunlun Fault, Northern Tibet. *Bull. Seismol. Soc. Am.* **2008**, *98*, 2866–2878. https://doi.org/10.1785/0120070193.
29. Jia, Y.N.; Zhang, Y.Z.; Huang, C.C.; Wang, N.L.; Qiu, H.J.; Wang, H.Y.; Xiao, Q.L.; Chen, D.; Lin, X.; Zhu, Y.; et al. Late Pleistocene-Holocene aeolian loess-paleosol sections in the Yellow River source area on the northeast Tibetan Plateau: Chronostratigraphy, sediment provenance, and implications for paleoclimate reconstruction. *Catena* **2022**, *208*, 105777. https://doi.org/10.1016/j.catena.2021.105777.
30. Wang, W.; Sun, M.; Che, Y.; Yao, X.; Zhang, M.; Niu, S. Micrometeorological Analysis and Glacier Ablation Simulation in East Kunlun. Water 2023, 15, doi:10.3390/w15193517.
31. Liu, X.Q.; Dong, H.L.; Yang, X.D.; Herzschuh, U.; Zhang, E.L.; Stuut, J.B.W.; Wang, Y.B. Late Holocene forcing of the Asian winter and summer monsoon as evidenced by proxy records from the northern Qinghai-Tibetan Plateau. *Earth Planet. Sci. Lett.* **2009**, *280*, 276–284. https://doi.org/10.1016/j.epsl.2009.01.041.
32. The Second Regional Geological Survey Team of Qinghai Province, The Institute of Crustal Dynamics of China Earthquake. Report on Regional Geological Survey of the People's Republic of China, Guoluo Tibetan Autonomous Prefecture and Youyun Community Assemblage with Scale 1:200,000, Geological Part; The Second Regional Geological Survey Team of Qinghai Province, The Institute of Crustal Dynamics of China Earthquake: Qinghai, China, 1986; pp. 210–221. (In Chinese)
33. Jing, G.Z.; Wang, X.Y.; Zhang, Z.Q.; He, J.J.; Zhang, L.B.; Wang, F.L.; Liu, Y.; Shi, W.J.; Tan, J. Middle-LateTriassic regional-scale magmatic-hydrothermal metallogenic system in the eastern segment of the East Kunlun. Bulletin of Geological Science and Technology 2023, 42, 89-111, doi:10.19509/j.cnki.dzkq.2022.0207.
34. Zhang, J.; Yu, M.; Wang, H.; Li, B.; Feng, C.; Dick, J.M.; Li, J.; Kong, H.; Zhao, Z. Geodynamic Setting and Cu-Ni Potential of Late Permian Xiwanggou Mafic-Ultramafic Rocks, East Kunlun Orogenic Belt, NW China. Frontiers in Earth Science 2021, 9, doi:10.3389/feart.2021.666967.
35. Tang, X.; Liu, S.; Zhang, D.; Wang, G.; Luo, Y.; Hu, S.; Xu, Q.; Billi, A. Geothermal Accumulation Constrained by the Tectonic Transformation in the Gonghe Basin, Northeastern Tibetan Plateau. Lithosphere 2022, doi:10.2113/2022/3936881.
36. Liu, Z.W.; Zhao, W.J.; Wu, Z.H.; Shi, D.N.; Song, Y.; Deng, S.G. East Kunlun Orogeny's uplift uncovered by deep reflection seismic data in INDEPTH IV. CHINESE JOURNAL OF GEOPHYSICS 2016, 59, doi:10.6038/CJG20160907.
37. Tozer, B.; Sandwell, D.T.; Smith, W.H.F.; Olson, C.; Beale, J.R.; Wessel, P. Global Bathymetry and Topography at 15 Arc Sec: SRTM15+. *Earth Space Sci.* **2019**, *6*, 1847–1864. https://doi.org/10.1029/2019ea000658.
38. Qu, C.Y. Builing to the active tectonic database of china. *Seismol. Geol.* **2008**, *30*, 298–304. https://doi.org/10.3969/j.issn.0253-4967.2008.01.022.

Preprints.org (www.preprints.org) | NOT PEER-REVIEWED | Posted: 19 March 2024 doi:10.20944/preprints202403.1101.v1

39. Lu, C.; Zhou, X.C.; Li, Y.; Liu, L.; Yan, Y.C.; Xu, Y.R. Hydrogeochemical characteristics of groundwater in the surface rupture zone of Madoi Ms earthquake and hot springs in the east Kunlun Fault. SEISMOLOGY AND GEOLOGY 2021, 43, 25, doi:10.3969/j.issn.0253-4967.2021.05.005.
40. Woith, H.; Wang, R.J.; Maiwald, U.; Pekdeger, A.; Zschau, J. On the origin of geochemical anomalies in groundwaters induced by the Adana 1998 earthquake. *Chem. Geol.* **2013**, *339*, 177–186. https://doi.org/10.1016/j.chemgeo.2012.10.012.
41. Chen, Z.; Zhou, X.; Du, J.; Xie, C.; Liu, L.; Li, Y.; Yi, L.; Liu, H.; Cui, Y. Hydrochemical characteristics of hot spring waters in the Kangding district related to the Lushan M_S = 7.0 earthquake in Sichuan, China. *Nat. Hazards Earth Syst. Sci.* **2015**, *15*, 1149–1156. https://doi.org/10.5194/nhess-15-1149-2015.
42. Zhou, R.; Zhou, X.C.; Li, Y.; He, M.; Li, J.C.; Dong, J.N.; Tian, J.; Li, K.Y.; Yan, Y.C.; Ouyang, S.P.; et al. Hydrogeochemical and Isotopic Characteristics of the Hot Springs in the Litang Fault Zone, Southeast Qinghai-Tibet Plateau. *Water* **2022**, *14*, 1496. https://doi.org/10.3390/w14091496.
43. Podlesak, D.W.; Torregrossa, A.M.; Ehleringer, J.R.; Dearing, M.D.; Passey, B.H.; Cerling, T.E. Turnover of oxygen and hydrogen isotopes in the body water, CO2, hair, and enamel of a small mammal. *Geochim. Cosmochim. Acta* **2008**, *72*, 19–35. https://doi.org/10.1016/j.gca.2007.10.003.
44. Li, Q.Y.; Wu, J.L.; Shen, B.B.; Zeng, H.; Li, Y.H. Water Chemistry and Stable Isotopes of Different Water Types in Tajikistan. *Environ. Process.-Int. J.* **2018**, *5*, S127–S137. https://doi.org/10.1007/s40710-018-0312-9.
45. Pang, Z.H.; Kong, Y.L.; Li, J.; Tian, J. An isotopic geoindicator in the hydrological cycle. In Proceedings of the 15th Water–rock Interaction International Symposium (WRI), Evora, Portugal, 16–21 October 2016; pp. 534–537.
46. Giggenbach, W.F. Isotopic shifts in waters from geothermal and volcanic systems along convergent plate boundaries and their origin. *Earth Planet Sci. Lett.* **1992**, *113*, 495–510. https://doi.org/10.1016/0012-821x(92)90127-h.
47. Ma, Z.; Yu, J.; Su, Y.; Xie, J.; Jia, X.; Hu, Y. δ18O shifts of geothermal waters in the central of Weihe Basin, NW China. *Environ. Earth Sci.* **2009**, *59*, 995–1008. https://doi.org/10.1007/s12665-009-0092-7.
48. Claesson, L.; Skelton, A.; Graham, C.; Morth, C.M. The timescale and mechanisms of fault sealing and water–rock interaction after an earthquake. *Geofluids* **2007**, *7*, 427–440. https://doi.org/10.1111/j.1468-8123.2007.00197.x.
49. Blasch, K.W.; Bryson, J.R. Distinguishing sources of ground water recharge by using delta H-2 and delta O-18. *Ground Water* **2007**, *45*, 294–308. https://doi.org/10.1111/j.1745-6584.2006.00289.x.
50. Liu, J.; Song, X.; Yuan, G.; Sun, X.; Liu, X.; Wang, S. Characteristics of δ 18O in precipitation over Eastern Monsoon China and the water vapor sources. *Chin. Sci. Bull.* **2009**, *55*, 200–211. https://doi.org/10.1007/s11434-009-0202-7.
51. Craig, H. Isotopic Variations in Meteoric Waters. *Science* **1961**, *133*, 1702–1703. https://doi.org/10.1126/science.133.3465.1702.
52. Ren, W.; Yao, T.; Yang, X.; Joswiak, D.R. Implications of variations in $\delta^{18}O$ and δD in precipitation at Madoi in the eastern Tibetan Plateau. *Quat. Int.* **2013**, *313–314*, 56–61. https://doi.org/10.1016/j.quaint.2013.05.026.
53. Seyfried, W.E.; Chen, X.; Chan, L.H. Trace element mobility and lithium isotope exchange during hydrothermal alteration of seafloor weathered basalt: An experimental study at 350 degrees C, 500 bars. *Geochim. Cosmochim. Acta* **1998**, *62*, 949–960. https://doi.org/10.1016/s0016-7037(98)00045-3.
54. Shand, P.; Darbyshire, D.P.F.; Love, A.J.; Edmunds, W.M. Sr isotopes in natural waters: Applications to source characterisation and water–rock interaction in contrasting landscapes. *Appl. Geochem.* **2009**, *24*, 574–586. https://doi.org/10.1016/j.apgeochem.2008.12.011.
55. Shakeri, A.; Ghoreyshinia, S.; Mehrabi, B.; Delavari, M. Rare earth elements geochemistry in springs from Taftan geothermal area SE Iran. *J. Volcanol. Geotherm. Res.* **2015**, *304*, 49–61. https://doi.org/10.1016/j.jvolgeores.2015.07.023.
56. Giggenbach, W.F. Geothermal solute equilibria. Derivation of Na-K-Mg-Ca geoindicators. *Geochim. Cosmochim. Acta* **1988**, *52*, 2749–2765.
57. Liu, J.H.; Zhang, S.Q.; Zhang, P.F.; Peng, Y. On the Lithogeochemical Features of the Upper Triassic Sequence Strata in West Sichuan. *Sichuan J. Geol.* **2005**, 198-201. (In Chinese)
58. Liu, T.J. Geologic Features, Provenance Nature and Tectonic Signigicance of Hongshuichuan Formation Located in the Southern Slope of the East Kunlun Orogenic Belt (Eastern Part). Master's Thesis, Chang'an University, Xi'an, China, 2015.
59. Yang, J.S.; Shi, R.D.; Wu, C.L.; Wang, X.B.; Robinson, P.T. Dur'ngoi Ophiolite in East Kunlun, Northeast Tibetan Plateau: Evidence for Paleo-Tethyan Suture in Northwest China. *J. Earth Sci.* **2009**, *20*, 303–331. https://doi.org/10.1007/s12583-009-0027-y.
60. Cai, C.F.; Franks, S.G.; Aagaard, P. Origin and migration of brines from Paleozoic strata in Central Tarim, China: Constraints from 87Sr/86Sr, dD, d18O and water chemistry. *Appl. Geochem.* **2001**, *16*, 1269–1284.
61. Wang, J.L.; Zhou, X.C.; He, M.; Li, J.C.; Dong, J.Y.; Tian, J.; Yan, Y.C.; Li, Y.; Liu, K.Y.; Li, Y. Hydrogeochemical origin and circulation of spring waters along the Karakorum fault, Western Tibetan

Preprints.org (www.preprints.org) | NOT PEER-REVIEWED | Posted: 19 March 2024 doi:10.20944/preprints202403.1101.v1

Plateau: Implications for interaction between hydrosphere and lithosphere. *Front. Earth Sci.* **2022**, *10*, 1021550. https://doi.org/10.3389/feart.2022.1021550.
62. Wang, C.G.; Zheng, M.P.; Zhang, X.F.; Wu, Q.; Liu, X.F.; Ren, J.H.; Chen, S.S. Geothermal-type Lithium Resources in Southern Xizang, China. *Acta Geol. Sin.-Engl. Ed.* **2021**, *95*, 860–872. https://doi.org/10.1111/1755-6724.14675.
63. Barberio, M.D.; Gori, F.; Barbieri, M.; Billi, A.; Caracausi, A.; De Luca, G.; Franchini, S.; Petitta, M.; Doglioni, C. New observations in Central Italy of groundwater responses to the worldwide seismicity. *Sci. Rep.* **2020**, *10*, 17850. https://doi.org/10.1038/s41598-020-74991-0.
64. Phuong, N.K.; Harijoko, A.; Itoi, R.; Unoki, Y. Water geochemistry and soil gas survey at Ungaran geothermal field, central Java, Indonesia. *J. Volcanol. Geotherm. Res.* **2012**, *229*, 23–33. https://doi.org/10.1016/j.jvolgeores.2012.04.004.
65. Liu, W.P.; Cui, H.Q.; Liu, W.P.; Chen, X.X.; Li, Z.H. An analysis of the evolution trend and influencing factors of the groundwater flow field in the Sanjiang Plain. HYDROGEOLOGY & ENGINEERING GEOLOGY 2021, 48, doi:10.16030/j.cnki.issn.1000-3665.202008044.
66. Düşünür-Doğan, D.; Üner, S. Numerical simulation of groundwater flow and temperature distribution in Aegean Coast of Turkey. Journal of Earth System Science 2019, 128, doi:10.1007/s12040-019-1183-9.
67. Yu, L.; Rozemeijer, J.C.; van der Velde, Y.; van Breukelen, B.M.; Ouboter, M.; Broers, H.P. Urban hydrogeology: Transport routes and mixing of water and solutes in a groundwater influenced urban lowland catchment. Sci. Total Environ. 2019, 678, 288-300, doi:10.1016/j.scitotenv.2019.04.428.
68. Arnorsson, S. Chemical-equilibria in icelandic geothermal systems—Implications for chemical geothermometry investigations. *Geothermics.* **1983**, *12*, 119–128. https://doi.org/10.1016/0375-6505(83)90022-6.
69. Fournier, R.O.; Rowe, J.J. The deposition of silica in hot springs. *Bull. Volcanol.* **1966**, *29*, 585–587.
70. Li, W.Y.; Zhang, J.; Tang, X.C.; Tian, J.; Wang, Y.C.; Guo, Q. The deep geothermal structure of high-temperature hydrothermal activity region in western Sichuan Plateau: A geophysical study. *Chin. J. Geophys.-Chin. Ed.* **2018**, *61*, 2926–2936. https://doi.org/10.6038/cjg2018L0043.
71. Pang, Z.H.Y.; Luo, L. *Research Method of Reservoir Temperature in Geothermal Field*; Ding, Z.L., Ed.; Science Press: Beijing, China, 2013; pp. 219–242.
72. Fournier, R.O.; Truesdell, A.H. An empirical Na-K-Ca geothermometer for natural waters. *Geochim. Cosmochim. Acta* **1973**, *37*, 1255-1275.
73. Kharaka, Y.K.; Mariner, R.H. Chemical geothermometers and their application to formation waters from sedimentary basins. *Thermal History of Sedimentary Basins* **1989**, 99-117.
74. Pang, Y.; Zou, K.; Guo, X.; Chen, Y.; Zhao, J.; Zhou, F.; Zhu, J.; Duan, L.; Yang, G. Geothermal regime and implications for basin resource exploration in the Qaidam Basin, northern Tibetan Plateau. *J. Asian Earth Sci.* **2022**, *239*, 105400. https://doi.org/10.1016/j.jseaes.2022.105400.
75. Zhang, L.; Guo, L.; Zhou, X.; Yang, Y.; Shi, D.; Liu, Y. Temporal variations in stable isotopes and synchronous earthquake-related changes in hot springs. J. Hydrol. 2021, 599, 126–316.
76. Manga, M.; Wang, C.Y. Earthquake Hydrology. In *Treatise on Geophysics*; Science Press: Beijing, China, 2015; pp. 305–328.
77. Fulton, P.M.; Saffer, D.M. Potential role of mantle-derived fluids in weakening the San Andreas Fault. *J. Geophys. Res.-Solid Earth* **2009**, *114*, 15. https://doi.org/10.1029/2008jb006087.
78. Long, K.; Zhang, Z.Y.; Li, S.H.; Li, K.; Luo, Y. The roles of crack development and water in stress rotation and fault weakening. *Tectonophysics* **2022**, *823*, 229190. https://doi.org/10.1016/j.tecto.2021.229190.
79. Martinelli, G. Previous, Current, and Future Trends in Research into Earthquake Precursors in Geofluids. Geosciences 2020, 10, doi:10.3390/geosciences10050189.
80. Zhou, H.L.; Zhou, X.C.; Su, H.J.; Li, Y.; Liu, F.L.; Ouyang, S.P.; Yan, Y.C.; Bai, R.L. Hydrochemical Characteristics of Earthquake-Related Thermal Springs along the Weixi-Qiaohou Fault, Southeast Tibet Plateau. Water 2022, 14, 21, doi:10.3390/w14010132.
81. Zhou, X.C.; Liu, L.; Chen, Z.; Cui, Y.J.; Du, J.G. Gas geochemistry of the hot spring in the Litang fault zone, Southeast Tibetan Plateau. Appl. Geochem. 2017, 79, 17-26, doi:10.1016/j.apgeochem.2017.01.022.
82. Andren, M.; Stockmann, G.; Skelton, A.; Sturkell, E.; Morth, C.M.; Gudrunardottir, H.R.; Keller, N.S.; Odling, N.; Dahren, B.; Broman, C.; et al. Coupling between mineral reactions, chemical changes in groundwater, and earthquakes in Iceland. *J. Geophys. Res.-Solid Earth* **2016**, *121*, 2315–2337. https://doi.org/10.1002/2015jb012614.
83. Skelton, A.; Liljedahl-Claesson, L.; Wasteby, N.; Andren, M.; Stockmann, G.; Sturkell, E.; Morth, C.M.; Stefansson, A.; Tollefsen, E.; Siegmund, H.; et al. Hydrochemical Changes Before and After Earthquakes Based on Long-Term Measurements of Multiple Parameters at Two Sites in Northern IcelandA Review. *J. Geophys. Res.-Solid Earth* **2019**, *124*, 2702–2720. https://doi.org/10.1029/2018jb016757.
84. Toutain, J.P.; Munoz, M.; Poitrasson, F.; Lienard, A.C. Springwater chloride ion anomaly prior to a ML = 5.2 Pyrenean earthquake. *Earth Planet. Sci. Lett.* **1997**, *149*, 113–119.

Preprints.org (www.preprints.org) | NOT PEER-REVIEWED | Posted: 19 March 2024 doi:10.20944/preprints202403.1101.v1

85. Zhao, D.Y.; Zhou, X.C.; Zhang, Y.X.; He, M.; Tian, J.; Shen, J.F.; Li, Y.; Qiu, G.L.; Du, F.; Zhang, X.M.; et al. Hydrogeochemical Study of Hot Springs along the Tingri-Nyima Rift: Relationship between Fluids and Earthquakes. *Water* **2023**, *15*, 1634. https://doi.org/10.3390/w15081634.
86. Reddy, D.V.; Nagabhushanam, P.; Sukhija, B.S. Earthquake (M 5.1) induced hydrogeochemical and δ18O changes: Validation of aquifer breaching-mixing model in Koyna, India. *Geophys. J. Int.* **2011**, *184*, 359–370. https://doi.org/10.1111/j.1365-246X.2010.04838.x.
87. Giuseppe, E.; Massimo, C.; Fedora, Q. Seismogeochemical algorithms for earthquake prediction: An overview. *Ann. Geophys.* **1997**, *40*, 1483–1492.
88. Martinelli, G.; Tamburello, G. Geological and Geophysical Factors Constraining the Occurrence of Earthquake Precursors in Geofluids: A Review and Reinterpretation. *Front. Earth Sci.* **2020**, *8*, 9. https://doi.org/10.3389/feart.2020.596050.
89. Pang, Z.H.; Luo, J.; Cheng, Y.Z.; Duan, Z.F.; Tian, J.; Kong, Y.L.; Li, Y.M.; Hu, S.B.; Wang, J.Y. Evaluation of geological conditions for the development of deep geothermal energy in China *Earth Sci. Front.* **2020**, *27*, 134–151. https://doi.org/10.13745/j.esf.2020.1.15. (In Chinese)

Disclaimer/Publisher's Note: The statements, opinions and data contained in all publications are solely those of the individual author(s) and contributor(s) and not of MDPI and/or the editor(s). MDPI and/or the editor(s) disclaim responsibility for any injury to people or property resulting from any ideas, methods, instructions or products referred to in the content.